

Characterisation and Quantum Application of Plasmonic Waveguides



Jason Tarunesh Francis

School of Chemistry and Physics

University of KwaZulu-Natal

A thesis submitted in fulfillment of the requirements for the degree of

Master of Science

December, 2016

Abstract

Plasmonics offers sub-diffraction confinement of light, which affords enhanced coupling to emitter systems (e.g. quantum dots). This feature makes possible a range of on-chip quantum photonic components - most notably single-photon sources and switches. This potential use of plasmonics, along with the nonlinearity provided by emitter systems, opens up quantum plasmonics as a viable route to realising quantum information processing. In this setting, the excitation of single surface plasmon polaritons (SPPs) on waveguides via single photons and the confirmation of single-photon states upon output is an important goal. In the work reported here, plasmonic waveguides were experimentally probed with single photons. A measurement of the second-order quantum coherence function yielded a value of $g^{(2)}(0) = 0.160 \pm 0.002$. A value less than 0.5 is indicative of single-excitation states. Furthermore, to confirm successful SPP excitation, the transverse-magnetic mode restriction and exponential decay of SPPs were verified. Having firmly established the ability to probe plasmonic waveguides in the classical and quantum regimes, quantum random number generation was implemented using a plasmonic beam splitter. The random bit sequences produced passed the NIST Statistical Test Suite once post-processed to correct for a slightly asymmetric beamsplitter.

Preface

The work reported in this dissertation was experimental in nature, and was carried out in the School of Chemistry and Physics, University of KwaZulu-Natal, under the supervision of Prof. Mark Tame.

As the candidate's supervisor I have approved this dissertation for submission.

Prof. M.S. Tame

Date

Declaration

I, Jason Tarunesh Francis declare that

1. The research reported in this thesis, except where otherwise indicated, is my original research.
2. This thesis has not been submitted for any degree or examination at any other university.
3. This thesis does not contain other persons' data, pictures, graphs or other information, unless specifically acknowledged as being sourced from other persons.
 - (a) This thesis does not contain other persons' writing, unless specifically acknowledged as being sourced from other researchers. Where other written sources have been quoted, then:
 - (b) Their words have been re-written but the general information attributed to them has been referenced; Where their exact words have been used, their writing has been placed inside quotation marks, and referenced.
4. This thesis does not contain text, graphics or tables copied and pasted from the Internet, unless specifically acknowledged, and the source being detailed in the thesis and in the References sections.

Signed: _____

Manuscripts

At the time of writing, two manuscripts were prepared:

1. Jason Francis and Mark Tame, Single-photon probing of plasmonic waveguides, submitted for publication in the Proceedings of the 61st annual conference of The South African Institute of Physics (2016).
2. Jason Francis, Xia Zhang, Şahin K. Özdemir, and Mark Tame, Quantum random number generation using an on-chip plasmonic beamsplitter, submitted for review, preprint available at <https://arxiv.org/abs/1610.06300>, (2016).

My contribution: I conducted all experimental aspects, data processing and analysis, wrote the related sections of paper 2 and the entirety of paper 1.

Acknowledgements

Gratitude goes to Prof. Mark Tame, from whom I have learnt much, for allowing creative freedom tempered with practicality. Sharmini Pillay, Marco Mariola, Yaseera Ismail and Maria Schuld have my deepest gratitude for the counsel they have offered me during the tenure of this research.

A thank you goes to Xia Zhang for providing me with atomic force microscope images, and to Yannick Seis for setting up the single-photon counting electronics.

This work is supported by the South African National Research Foundation, Department of Science and Technology, National Laser Centre, and the UKZN Nanotechnology Platform.

Contents

1	Introduction	13
1.1	Background	13
1.2	Aim and Approach	15
1.3	Outline	16
2	Surface Plasmon Polaritons	17
2.1	Classical Description	17
2.2	Coupling Strategies	21
2.2.1	Gratings	21
2.2.2	Prisms	21
2.2.3	End-firing	21
2.3	Quantum Description	22
3	Light Sources	24
3.1	Classical Light Sources	24
3.2	Quantum Source	26
3.2.1	Characterisation	26
3.2.2	Experimental Setup	28
3.2.3	Results and Discussion	29
4	Stripe Waveguides: Simulations	31
4.1	Grating Optimisation	32
4.1.1	Period and Height Optimisation	32
4.1.2	Period and Duty-cycle Optimisation	33
4.2	Characterisation	34
4.2.1	Polarisation Dependence	35
4.2.2	Decay Length	35
4.2.3	Spectral Response	36

4.3	Out-coupling Simulations	37
5	Stripe Waveguides: Experiments	40
5.1	Experimental Setup	40
5.2	Characterisation	42
5.2.1	Classical	44
5.2.2	Quantum	45
5.3	Results and Discussion	46
5.3.1	Classical	46
5.3.2	Quantum	47
5.4	Summary	49
6	Quantum Random Number Generation	50
6.1	Introduction	50
6.2	Experimental Details	51
6.3	Initial Characterisation	53
6.4	Post-processing	55
6.5	Results	56
6.6	Discussion	56
7	Summary	58

List of Figures

2.1	Two-layer geometry supporting SPPs.	18
2.2	SPP dispersion curve for a silver-air interface.	20
2.3	Grating and prism coupling schemes.	22
3.1	Filter characterisation: Setup.	25
3.2	Filter characterisation: Spectral response.	25
3.3	Single-photon source setup	28
3.4	Second-order coherence coefficient against time delay of heralded photons filtered by an 810nm IF.	30
3.5	Second-order coherence function against time delay of heralded photons filtered by an 800nm IF.	30
4.1	Waveguide geometry showing parameters considered for optimisation. The coordinate system is chosen differently to that introduced in the theory of Chapter 2 due to convenience in design when using COMSOL.	32
4.2	Period-Height optimisation	33
4.3	Period-DC optimisation	34
4.4	Simulated polarisation dependence plots	35
4.5	Simulated SPP decay plots	36
4.6	Simulated response of input gratings	37
4.7	Geometry of out-coupling simulations	38
4.8	Simulated out-coupling transmission plots	39
5.1	Waveguide structure	41
5.2	Compound Microscope stage used to probe plasmonic waveguides.	42
5.3	Optical image of waveguide	42
5.4	AFM image of waveguides	43
5.5	Spectral response of $p = 700\text{nm}$ grating	45
5.6	Spectral response of $p = 740\text{nm}$ grating	46

5.7	Classical SPP characterisation plots	47
5.8	Single-SPP characterisation plots	48
5.9	Plasmonic output count rates	49
5.10	Plasmonic $g^{(2)}(0)$ as a function of integration time	49
6.1	Quantum random number generation setup	51
6.2	Characterisation of generated random bit sequence	54

List of Tables

3.1	Count rates produced by single-photon source.	29
4.1	Polarisation dependence fit parameters	35
4.2	Simulated SPP decay lengths	36
6.1	Summary of results from tests applied to the post-processed and PRNG sequences.	56
6.2	Summary of results from the NIST tests applied to the post-processed sequence QRNG	57

Chapter 1

Introduction

1.1 Background

Plasmonics is the study of the interaction of light and conduction electrons at metal-dielectric interfaces. Charge density oscillations (plasmons) within the metal may couple to the external electromagnetic field resulting in hybrid photon-electron excitations [1]. Such plasmonic fields are confined to the interface at sub-diffraction scales [2, 3], and are sensitive to the refractive index of the dielectric medium. One such field, surface plasmon polaritons (SPPs), are surface waves that propagate along the interface. The dispersion relation of SPPs are such that for a photon with angular frequency of ω and wavevector magnitude k_0 , the corresponding SPP has $k_{SPP} > k_0$ [1]. Thus a SPP has a smaller wavelength and greater momentum than a freespace photon of the same frequency. This mismatch requires that phase-matching techniques be employed for photon-SPP mode conversion. Another class of plasmonic fields are localised surface plasmons (LSPs). These are non-propagating modes on the surface of conductive nanoparticles. The free electrons in metallic nanoparticles have a natural frequency for collective oscillation that depends on material properties and geometry. When incident light at this resonant frequency scatters on the nanoparticle, LSPs can be excited. LSPs, unlike SPPs, do not require phase-matching for excitation [1]. This along with higher confinement may make LSPs more attractive if a guided mode is not needed. Ultimately, preference is dictated by the specific requirements of the application.

The intense and highly confined light, refractive index sensitivity, and the small scale afforded by plasmonic systems has proved advantageous in some important applications. For instance:

1. **Optical nano-imaging** [4]: Traditional dielectric microscope objectives suffer from the diffraction limit $d = \frac{\lambda}{2n\sin\theta}$ [5]. Here n is the refractive index of the medium, θ is the numerical aperture of the objective, and λ is the probing wavelength. The minimum resolvable distance d is at best of the order

of $\sim 100 \text{ nm}$ for visible light. SPPs and LSPs allow us to improve the resolution by reducing λ while still maintaining the frequency. An object placed on a metal surface supporting SPPs will scatter light which can be collected by a microscope objective to form an image [6].

2. **Nano-sensing** [7, 8]: Sensing applications are aided by the refractive index sensitivity of LSPs. For example, the presence of a biomolecule present in the dielectric medium causes small changes in the refractive index. These small changes results in measurable shifts of the LSP resonance wavelength.
3. **Electro-optic circuits** [9]: The integration of electronic and (dielectric) photonic circuitry is made difficult by the difference in scale. Plasmonic elements with dimensions of the order of $10 \text{ nm} - 100 \text{ nm}$ can be used and are more suitable.
4. **Optical metamaterials** [10, 11]: Plasmonic meta-materials are an array of unit structures (cells) which consist of sub-wavelength metal antennae supporting LSPs. These unit cells can be designed and arranged so that the meta-material possesses optical properties, such as a negative refractive index, which are not seen in traditional materials.

Despite the macroscopic nature of charge density waves, SPPs are quasi-particles and exhibit quantum effects. There has been much research activity geared towards uncovering the quantum properties of SPPs and their potential for quantum technology [12]. Of particular interest is the application to quantum information processing and computation (QIPC). Here quantum plasmonics offers an alternative to a purely photonic realisation. A major advantage it offers is the sub-diffraction confinement of plasmonic modes. This allows enhanced coupling of light to emitter systems, such as nitrogen vacancy centres [13] and quantum dots [14], by reducing the large size discrepancy between the modes. This strong coupling makes on-chip single-photon and single-SPP sources possible [15–18]. Additionally, it can provide nonlinearity via a photon-blockade [19], where an emitter excited by a photon of a particular frequency cannot be further excited. This process has application in the development of active switches [20–22], which are useful for implementing controlled quantum logic gates.

To further motivate the suitability of SPPs for QIPC, several demonstrations have been made suggesting that photonic entanglement and quantum information can indeed be encoded in plasmonic states [12]. These include:

1. **Wave-particle duality** [16]: In this experiment a single-photon emitter (nitrogen vacancy centre) was coupled to a metal nanowire. When the emitter decays SPPs are excited on the nanowire. The experiment demonstrated that the excitations would decouple from one of either end of the wire and not both, indicating a particle nature. The wave nature of the SPPs manifested as interference fringes in the spectra of the photons decoupled at either end of the wire. This shows that single-SPPs self-interfered on the nanowire.
2. **Entanglement**: It was first shown that polarisation-entangled photon pairs maintain entanglement after

conversion to and from SPPs [23]. In this demonstration, a photon from each pair underwent conversion using a two-dimensional periodic array of holes on a metal film. The periodicity of the grid met the necessary phase-matching requirements to excite SPPs which then propagated through the holes. Upon reaching the end the photons were decoupled and found to be entangled (though to a lesser degree). Further demonstration were then made for time-energy [24] and orbital angular momentum entanglement [25]. Again a similar grid of holes were used. In ref. [24] however, long-ranged surface plasmons on a metallic stripe waveguide also exhibited entanglement preservation.

3. **Photon-number statistics** [26]: The authors excited heralded SPPs on a metallic stripe waveguide using single photons generated via spontaneous parametric down-conversion (SPDC) [27, 28]. The second-order coherence function [28–30] was obtained for the heralded photons before conversion to SPPs. The result indicated that single photons were indeed being used. The same measurement was then performed after the waveguide on the out-coupled photons. Again the result showed single excitations, confirming that SPPs preserve the number statistics of their exciting photons.
4. **Quantum interference**: Two-SPP interference has been shown to exhibit the Hong-Ou-Mandel effect [31], which confirms the bosonic nature of single SPPs. The single SPPs were excited by single photons, and interfered in plasmonic directional-couplers [32–34] and a beamsplitter-type waveguide [35].

Plasmonic systems are well known to be inherently lossy [1] and as such their application to quantum information processing is not well developed at this stage. So far, theoretical studies have shown that entanglement can be generated via plasmonic waveguides even in the presence of loss, either by using it as a resource [36, 37], or circumventing it by appropriate methods [38]. By using special encoded quantum states it has also been shown that one can propagate quantum information over arbitrary distances on lossy plasmonic waveguides [39]. Most recently, it has been shown that the sensitivity in plasmonic sensing can be enhanced even in the presence of loss [40]. It is therefore clear that despite the presence of loss, plasmonics can still exploit quantum effects and carry out useful quantum tasks, but with the added benefit that this is done at a much smaller scale than conventional photonics. This makes plasmonics an attractive platform for certain types of nanophotonic QIPC.

1.2 Aim and Approach

The main goal of the project was to develop the experimental capacity to explore further the quantum properties of plasmonic systems and their application to QIPC. Of particular interest for future work is to experimentally investigate emitters coupled to plasmonic structures. As a first step on this path, we follow the lead of Di Martino et al. [26]. We couple heralded single photons into SPP modes on plasmonic stripe waveguides, and confirm single excitation states upon decoupling by a measurement of the second-order coherence function at

zero time delay $g^{(2)}(0)$ [29]. In order to verify SPP excitation, two characteristics of SPPs are demonstrated. These are the exponential intensity decay of SPPs as they propagate, and that they are transverse-magnetic (TM) modes [1]. This is done in both classical and quantum regimes. In performing these experiments we demonstrate acquirement of the crucial skills and facilities needed for further and more novel studies. We then emphasise the use of plasmonics for QIPC by demonstrating quantum random number generation using a plasmonic beamsplitter.

The experimental work undertaken was supplemented with a review of the relevant background theory. Additionally, numerical simulations of SPP excitation were performed. Such simulations are a common tool used to study plasmonic structures before fabrication and experimental probing.

1.3 Outline

- We begin first with a description of SPPs in the classical and quantum regimes in Chapter 2, along with a look at excitation methods.
- This is followed by a characterisation of all light sources used during this project in Chapter 3. It is here that details on the second-order coherence function are presented as well as the experimental SPDC setup.
- Before embarking on the experimental probing of plasmonic stripe waveguides, a series of light-to-SPP coupling simulations were run (Chapter 4). These simulations were used to determine which of the available waveguides were most suitable for our purposes.
- The experimental characterisation of selected waveguides is then presented in Chapter 5. This involves:
 1. Verifying the TM mode restriction and exponential decay of the supported SPPs in the classical and quantum regimes.
 2. The spectral response of the waveguides classically.
 3. The photon-number preserving property of SPPs.
- We then demonstrate a simple application of plasmonic waveguides in quantum random number generation. The introduction of this topic has been left to Chapter 6, which also contains the appropriate experimental details and analysis.
- Finally in Chapter 7, the project is summarised and the future outlook is discussed.

Chapter 2

Surface Plasmon Polaritons

Many aspects of plasmonics are well described by classical electrodynamics. Using Maxwell's equations, we derive the classical field expressions for SPPs supported by a single interface. In doing so, we will show the SPP characteristics: that they are transverse-magnetic, decay exponentially with propagation, and are evanescently confined to the interface. Another important result derived is the SPP dispersion relation. For photon-to-SPP coupling, the dispersion relation affirms the phase-matching requirement. In response, the following section presents descriptions of three coupling methods. The chapter concludes with a brief section outlining a basic quantisation procedure of lossless SPPs. It serves as a starting point for future work in quantum plasmonics.

2.1 Classical Description

The derivation of the SPP field expressions presented here are based on the treatment found in Ref. [1]. We begin with the wave equation

$$\nabla^2 \mathbf{E} - \frac{\epsilon}{c^2} \frac{\partial^2 \mathbf{E}}{\partial t^2} = 0, \quad (2.1)$$

which can be derived from Maxwell's macroscopic equations with zero external charge and current densities. Here ϵ is the dielectric function describing the material in which the electric field \mathbf{E} resides, and c is the speed of light in vacuum. Assuming harmonic time-dependence, we can write $\mathbf{E}(\mathbf{r}, t) = \mathbf{E}(\mathbf{r})e^{-i\omega t}$. Substituting this into Eqn. 2.1 yields the Helmholtz equation:

$$\nabla^2 \mathbf{E} + k_0^2 \epsilon \mathbf{E} = 0 \quad (2.2)$$

where $k_0 = \frac{\omega}{c}$ is the freespace propagation constant given here in terms of angular frequency. We consider the two-dimensional two-layer geometry shown in Fig. 2.1 in which each layer is an infinite half-space. The surface waves propagate along the x -direction and are constant in y . Hence $\mathbf{E}(\mathbf{r}) = \mathbf{E}(z)e^{ik_x x}$, where k_x is the wave vector component parallel to the interface. Substituting this form into Eq. 2.2 we arrive at:

$$\frac{\partial^2 \mathbf{E}(z)}{\partial z^2} + (k_0^2 \epsilon - k_x^2) \mathbf{E}(z) = 0. \quad (2.3)$$

Similarly, we can obtain the equation for the magnetic field $\mathbf{H}(z)$,

$$\frac{\partial^2 \mathbf{H}(z)}{\partial z^2} + (k_0^2 \epsilon - k_x^2) \mathbf{H}(z) = 0. \quad (2.4)$$

Equations 2.3 and 2.4 can be solved for the field amplitudes and the SPP propagation constant k_x . Differential equations from which we can solve for each field component can be obtained from Maxwell's curl equations:

$$\nabla \times \mathbf{E}(\mathbf{r}, t) = -\mu_0 \frac{\partial \mathbf{H}(\mathbf{r}, t)}{\partial t}, \quad (2.5)$$

$$\nabla \times \mathbf{H}(\mathbf{r}, t) = \epsilon_0 \epsilon \frac{\partial \mathbf{E}(\mathbf{r}, t)}{\partial t}, \quad (2.6)$$

where ϵ_0 and μ_0 are the freespace permittivity and permeability respectively. Carrying out the differentiation in equations 2.5 and 2.6 using $\nabla = ik_x \hat{x} + \frac{\partial}{\partial z} \hat{z}$ and $\frac{\partial}{\partial t} = -i\omega$ yields:

$$-\frac{\partial E_y}{\partial z} \hat{x} + \left(\frac{\partial E_x}{\partial z} - ik_x E_z \right) \hat{y} + ik_x E_y \hat{z} = i\omega \mu_0 (H_x, H_y, H_z), \quad (2.7)$$

$$-\frac{\partial H_y}{\partial z} \hat{x} + \left(\frac{\partial H_x}{\partial z} - ik_x H_z \right) \hat{y} + ik_x H_y \hat{z} = -i\omega \epsilon_0 \epsilon (E_x, E_y, E_z). \quad (2.8)$$

There exist two solution sets that ensure that the electric and magnetic vectors reside in orthogonal planes; a transverse-magnetic (TM) and transverse-electric (TE) mode. For a TM mode ($H_x = H_z = E_y = 0$), we can

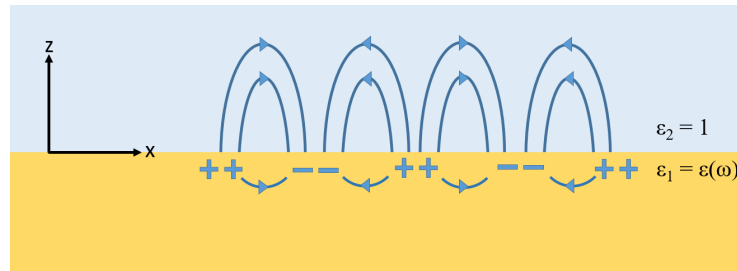


Figure 2.1: Two-layer geometry for which the SPP field equations are solved. The region $z < 0$ is metallic with complex dielectric function $\epsilon(\omega)$. The dielectric region ($z > 0$) is air with $\epsilon = 1$. The interface between the regions, $z = 0$, supports the SPPs illustrated by the electric field pattern.

extract E_x and E_z from equations 2.7 and 2.8, and use the wave equation 2.4 for H_y :

$$E_x = -\frac{i}{\omega\epsilon_0\epsilon} \frac{\partial H_y}{\partial z}, \quad (2.9)$$

$$E_z = -\frac{k_x}{\omega\epsilon_0\epsilon} H_y, \quad (2.10)$$

$$\frac{\partial^2 H_y}{\partial z^2} + (k_0^2\epsilon - k_x^2)H_y = 0. \quad (2.11)$$

Equations 2.9-2.11 must be solved in both regions separately since ϵ differs between them. In the air we take $\epsilon = \epsilon_2 = 1$. As for the metal, its dielectric function is strongly dependent on the frequency of light, hence we denote it as $\epsilon_1 = \epsilon(\omega)$. It is complex with a negative real part describing the optical response of the material, and an imaginary part describing absorptive loss. This function can be approximated by the Drude-Lorentz model,

$$\epsilon(\omega) = 1 + \frac{\omega_p^2}{\omega^2 + i\gamma_p\omega}, \quad (2.12)$$

where ω_p is the plasma frequency and γ_p is the electron collision frequency. Alternatively, it can be experimentally obtained [41, 42]. We begin with Eq. 2.11 by making the substitution:

$$k_j^2 = k_x^2 - k_0^2\epsilon_j, \quad (2.13)$$

where $j = 2$ for $z > 0$ (air) and $j = 1$ for $z < 0$ (metal). The solution appropriate for evanescent surface waves is of the form $e^{ik_x x} e^{\pm k_j z}$ - we take $+k_1$ for $z < 0$ and $-k_2$ for $z > 0$. Here k_j is the wave vector component perpendicular to the interface. We now have

$$H_y(x, z) = \alpha_j e^{ik_x x} e^{-k_z z}, \quad (2.14)$$

where $k_z = (-1)^j k_j$ and α_j is an amplitude. Then substituting Eq. 2.14 into 2.9 and 2.10 yields:

$$E_x(x, z) = i\alpha_j \frac{k_z}{\omega\epsilon_0\epsilon_j} e^{ik_x x} e^{-k_z z}, \quad (2.15)$$

$$E_z(x, z) = -\alpha_j \frac{k_x}{\omega\epsilon_0\epsilon_j} e^{ik_x x} e^{-k_z z}. \quad (2.16)$$

The electric field vector in each layer can be written as:

$$\mathbf{E}(\mathbf{r}, t) = \alpha_j \frac{k_z}{i\omega\epsilon_0\epsilon_j} e^{ik_x x} e^{-k_z z} \left(\hat{\mathbf{x}} - \frac{ik_x}{k_z} \hat{\mathbf{z}} \right) e^{-i\omega t}. \quad (2.17)$$

Enforcing continuity at $z = 0$ gives:

$$H_{y1} = H_{y2} \implies \alpha_1 = \alpha_2,$$

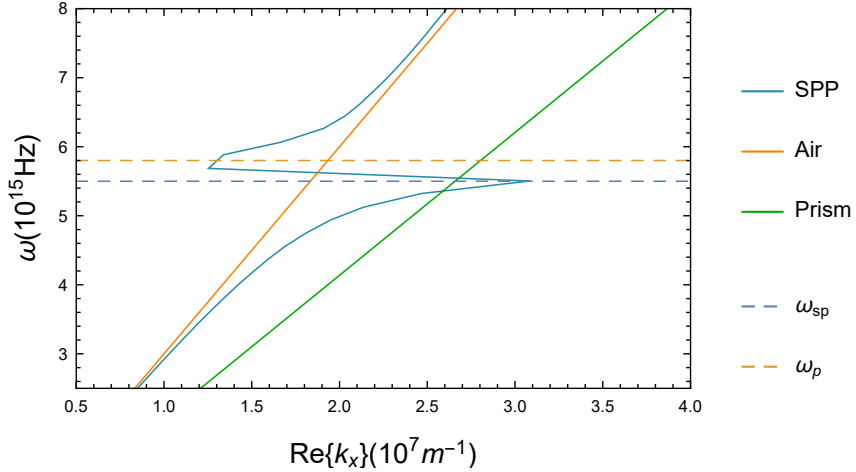


Figure 2.2: Dispersion curves for light in air and a dielectric prism, and SPPs on a silver-air interface. The dielectric function was calculated using the complex refractive index obtained by Johnson and Christy [41].

and

$$E_{x1} = E_{x2} \implies \frac{k_2}{k_1} = -\frac{\epsilon_2}{\epsilon_1}.$$

Using this last relation with Eq. 2.13, we arrive at the SPP dispersion relation:

$$k_x = k_0 \sqrt{\frac{\epsilon_1 \epsilon_2}{\epsilon_1 + \epsilon_2}} = k_0 \sqrt{\frac{\epsilon(\omega)}{\epsilon(\omega) + 1}}. \quad (2.18)$$

A plot of the SPP dispersion relation for a silver-air interface is shown in Fig. 2.2. The portion of the curve above the plasmon frequency ω_p corresponds to light radiating through the metal. The region below the surface plasmon frequency $\omega_{sp} = \frac{\omega_p}{\sqrt{1+\epsilon_2}}$ (obtained by inserting Eq. 2.12 for epsilon into Eq. 2.18 and taking the limit of large wavenumber) describes bound SPPs. The curve clearly deviates from the dispersion line of unguided light in freespace. Note that k_x is complex and $Re\{k_x(\omega)\} > k_0(\omega)$, hence SPPs have greater momentum than photons of the same frequency. This is most significant for ω close to ω_{sp} . k_{z1} and k_{z2} are also complex; their real parts describe decay while their imaginary parts describe propagation. The field's spatial intensity profile is characterised by three lengths:

- Propagation distance at which the intensity is e^{-1} of the original: $L = \frac{1}{2Im\{k_x\}}$.
- Evanescent decay into the air: $L_{air} = \frac{1}{2Im\{k_2\}}$.
- Evanescent decay into the metal: $L_{metal} = \frac{1}{2Im\{k_1\}}$.

A last SPP characteristic of interest is the TM mode restriction. In following the same procedure for TE modes as was done for TM, we find that the continuity conditions at the interface yield: $\alpha_1 = \alpha_2$ and $\alpha_1(k_{z1} + k_{z2}) = 0$. Since $Re\{k_x\} > k_0$ in Eq. 2.13, $Re\{k_{z1}\}$ and $Re\{k_{z2}\}$ are both positive. Hence to satisfy the conditions $\alpha_1 = \alpha_2 = 0$, leading to no surface waves.

2.2 Coupling Strategies

As $k_{SPP} > k_0$, techniques to overcome the momentum mismatch are required for SPP excitation. There exist several such techniques, three of which are discussed in this section. The first two, grating and prism coupling, are common methods which employ phase-matching. Despite their prevalence, these methods do not lend themselves well for on-chip applications. The third method, end-firing, is more suitable, but has its own drawbacks.

2.2.1 Gratings

Consider a photon with wave vector \mathbf{k}_0 , incident on a dielectric-metal interface at angle θ . This photon cannot excite a SPP of the same frequency since the SPP has a propagation constant $k_{SPP} > |\mathbf{k}_0|\sin(\theta) = k_0\sin(\theta)$. A grating consisting of periodic arrays of scatterers on the interface can provide the photon with the missing momentum [1]. The grating illustrated in Fig. 2.3a has a period of p , and can thus provide the photon with additional momentum $\frac{h}{p}$ where h is Plank's constant. For successful coupling we require that θ and p be chosen such that,

$$k_{SPP} = k_0\sin(\theta) \pm \frac{2\pi n}{p}, \quad (2.19)$$

where $n \in \mathbb{Z}^+$, is satisfied. Note that this relation does not account for the effects of grating height (depth). It is only suitable for heights less than 20 nm [1, 44], but we may use it to give an estimate.

2.2.2 Prisms

Prism coupling (or attenuated total-internal reflection) makes use of a three layer dielectric-metal-dielectric geometry such as that shown in Fig. 2.3b [45]. One of the dielectric layers has a higher refractive index n_p and is typically a prism. As an example consider the upper dielectric layer to be air. An exciting beam incident at angle θ on the air-metal interface will have a parallel wave vector component of $k_{\parallel air} = k_0\sin(\theta) < k_{SPP}$. On the other hand, if the beam is incident on the prism-metal interface we have $k_{\parallel prism} = k_0n_p\sin(\theta) > k_{\parallel air}$. Thus the evanescent field produced upon total-internal reflection can tunnel through to the air-metal interface and couple to a SPP with $k_{SPP} = k_0n_p\sin(\theta)$. Such SPP modes lie between the air and prism dispersion lines shown in Fig. 2.2. Modes in this region suffer from leakage back into the prism, and shorter propagation distances as a result.

2.2.3 End-firing

The end-firing technique achieves photon-to-SPP coupling by matching the spatial profiles. Here the input beam is directed parallel to the SPP propagation direction, and is tightly focused onto the end of the waveg-

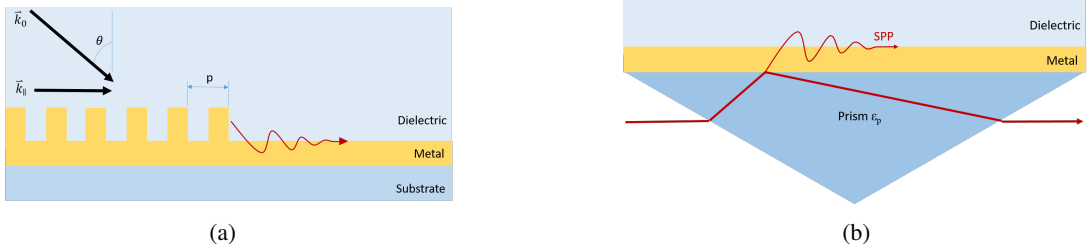


Figure 2.3: (a) Simple grating coupling geometry. Grating parameters such as shape, spacing, and height can all vary over distance to achieve different effects. (b) Kretschmann prism coupling configuration.

uide. The resulting SPPs are long ranged but poorly confined since the input beam cannot be focused down to sub-diffraction scales [1].

2.3 Quantum Description

The quantisation procedure outlined here involves the discretization of the vector potential $\mathbf{A}(\mathbf{r}, t) = -\frac{\partial \mathbf{E}(\mathbf{r}, t)}{\partial t}$. From Eq. 2.17 we have $\mathbf{A}(\mathbf{r}, t) = i\omega \mathbf{E}(\mathbf{r}, t)$. Generalising this for multi-mode fields, and a three-dimensional geometry in which the SPP interface coincides with the xy -plane, we have [46]:

$$\mathbf{A}(\mathbf{r}, t) = \frac{1}{(2\pi)^2} \int d^2\mathbf{k} \alpha_k \mathbf{u}_k(\mathbf{r}) e^{-i\omega t} + c.c. \quad (2.20)$$

Here *c.c.* denotes the complex conjugate of the first term, and $\mathbf{k} = k\hat{\mathbf{k}}$ is the SPP wave-vector with magnitude k given by E.q. 2.18. Only the real part of the metal layers dielectric function is taken, thereby neglecting loss. This is because quantisation must be carried out for a closed system, with the energy conserved. Loss effects are introduced later, transforming the SPP into an open quantum system. The factor α_k is the amplitude of mode k , and $\mathbf{u}_k(\mathbf{r})$ is given by

$$\mathbf{u}_k(\mathbf{r}) = \frac{1}{\sqrt{L(\omega)}} e^{i\mathbf{k}\cdot\mathbf{r}} e^{-k_j z} \left(\hat{\mathbf{k}} - \frac{i k}{k_j} \hat{\mathbf{z}} \right), \quad (2.21)$$

and are the mode functions which describe the spatial aspects of the electric field. In this expression $L(\omega)$ is a normalisation factor, and k_j is the familiar wave-vector normal to the interface given by E.q. 2.13. The positive and negative solutions of E.q. 2.13 are taken for the fields in air and the metal respectively. The mode functions are discretized by confining the surface waves to an area $S = L_x L_y$ on the interface. In doing so, the wavevector components become restricted to discrete values: $k_x = \frac{2\pi n_x}{L_x}$ and $k_y = \frac{2\pi n_y}{L_y}$ where $n_x, n_y \in \mathbb{Z}$. Replacing the integration over mode-surface in E.q. 2.20 by a summation, and then calculating the total energy in S yields,

$$U = \sum_{\mathbf{k}} \epsilon_0 \omega^2 S [\alpha_k \alpha_k^* + \alpha_k^* \alpha_k]. \quad (2.22)$$

Equation 2.22 has the same form as a harmonic oscillator, hence we can apply the quantisation rules $\alpha_k \rightarrow \sqrt{\hbar/2\epsilon_0\omega S}\hat{a}_k$ and $\alpha_k^* \rightarrow \sqrt{\hbar/2\epsilon_0\omega S}\hat{a}_k^\dagger$. The operators \hat{a}_k and \hat{a}_k^\dagger serve as SPP annihilation and creation operators respectively. They obey the commutation relation $[\hat{a}_k, \hat{a}_{k'}^\dagger] = \delta_{kk'}$.

The exponential loss incurred during propagation, due to electron-electron and electron-phonon scattering, can be modelled as an SPP interacting with bath modes to which it may be lost [48]. The strength of this interaction depends on the imaginary part of the metal layers dielectric function. This phenomenological approach is used as it is not possible to keep track of the dynamics of all the electrons and phonons involved. The result is an exponential decay in detection probability of the single SPP. This method is based on the beam splitter attenuation model in Ref. [29].

Chapter 3

Light Sources

In this chapter we describe several light sources used to probe plasmonic waveguides in the classical and quantum regimes. These sources were not exclusively used for SPP excitation in the experiments of later chapters. The roles they played will be explained in the following sections, the first of which briefly describes the classical sources. The second section is dedicated to the single-photon source, and is the main focus of this chapter.

3.1 Classical Light Sources

Descriptions of three continuous-wave (CW) lasers that served as classical light sources are listed below. Included here are the characterisation of two interference filters (IF). These are often used in conjunction with sources to select certain spectral regions.

1. Blue: A 200 *mW* solid-state laser (COHERENT OBIS) of peak wavelength (405 ± 2) *nm*. It has a Gaussian spatial profile and is vertically polarised ($\pm 5^\circ$). This laser is not used for SPP excitation. Instead, it is used as a component in the single source.
2. Red: A 10 *mW* diode laser (ThorLabs LPS-785-FC) with a typical peak wavelength of 780 *nm* with a full-width at half-maximum (FWHM) of 20 *nm*. The spectrum of this laser contains small components of 675 *nm* and 635 *nm* light, making it visible and suitable for alignments purposes.
3. White: A supercontinuum laser (Fianium WhiteLase Micro) with a wavelength range of 450 *nm* to 2000 *nm*. The total power across the spectrum is 200 *mW* with an average spectral power density of $50 \mu\text{W}.\text{nm}^{-1}$. Due to its broad spectrum, it is used to characterise the spectral response of components as is done below. Additionally, it can be used with a dispersive prism to serve as a lower-powered

tunable wavelength source. In future it will be used to identify nitrogen-vacancy centres in nano-diamond samples.

Two pairs of IFs were employed, one with a central transmission wavelength of 800 nm and a FWHM of 40 nm . The other was a 810 nm filter with a FWHM of 10 nm . These are as quoted on their specification sheets. The filters were characterised using the setup shown in Fig. 3.1. The broad spectrum of the white laser is attenuated using neutral density (ND) filters. The combination of ND filters were found to be most efficient at lower wavelengths resulting in the less uniform spectrum shown in Fig. 3.2a. It can be seen that the spectrum is fairly uniform over a region larger than 40 nm around 800 nm . This suggests that using this spectrum as an input, we may approximate the spectral responses of our IFs. To obtain these responses, we collect the light transmitted through both IFs individually. The light is coupled into a multimode (MM) optical fibre which is in turn connected to a spectrometer (ThorLabs CCS175). The spectra obtained for each filter is shown on Figs. 3.2b and 3.2c. From these we extract a central wavelength of 800 nm and a range of $(790 - 821)\text{ nm}$ at half-maximum for the wider filter. For the narrower filter we obtain a central wavelength of 812 nm and a FWHM of 10 nm . The discrepancies are due to off-normal incidence. The IFs were positioned at a slight angle to the incident beam to prevent reflected light from re-entering the laser.

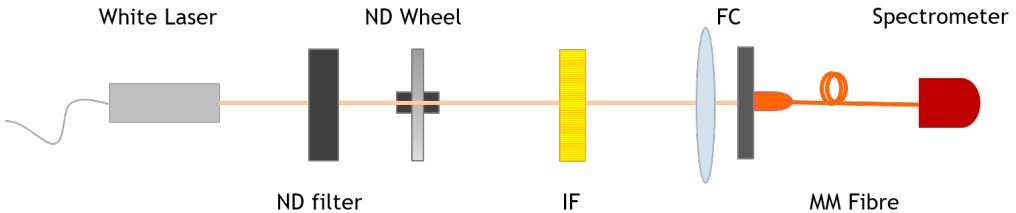


Figure 3.1: Filter characterisation setup.

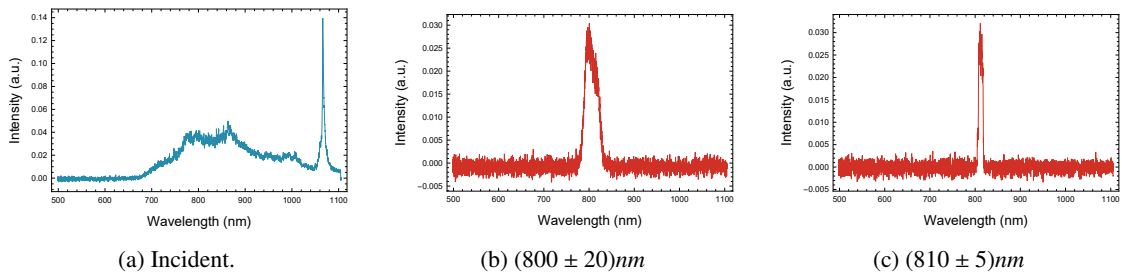


Figure 3.2: Spectral response of filters: (a) is the input spectrum to the filters resulting from the white laser passing through the fixed and variable ND filters. (b) and (c) are the approximate response of the $(800 \pm 20)\text{ nm}$ and $(810 \pm 5)\text{ nm}$ IF filters respectively.

3.2 Quantum Source

The single-photon source required to probe in the quantum regime was served by a spontaneous parametric down-conversion (SPDC) setup [28]. SPDC is a nonlinear optical process by which a photon of frequency ω_p from a pump beam is converted into a correlated photon-pair at lower frequencies and at particular angles relative to the pump. One photon of the pair is called the signal with frequency ω_s while the other is called the idler with frequency ω_i . The frequencies and angles of the output photons must satisfy the conservation of energy and momentum:

$$\omega_p = \omega_s + \omega_i \quad (3.1)$$

$$\mathbf{k}_p = \mathbf{k}_s + \mathbf{k}_i \quad (3.2)$$

where \mathbf{k}_p , \mathbf{k}_s , and \mathbf{k}_i , are the pump, signal, and idler wavevectors respectively. This results in a conical region in which time-correlated photons are located on opposite sides of the pump, which we label as modes *A* and *B* once detected, as shown in Fig. 3.3. Photon detections at *A* are used to herald the presence of a photon in mode *B*, in this manner we generate single photons. The photon-pairs produced are orthogonally polarised to the pump polarization. The Hamiltonian for this interaction is $\hat{H}_i = \hbar\eta a_s^\dagger a_i^\dagger + h.c.$, where a_s^\dagger and a_i^\dagger are the creation operators of the signal and idler beams respectively. The factor η is proportional to the classical field amplitude of the pump and the second order susceptibility of the nonlinear material (usually a crystal) [27]. Thus the probability of down-conversion occurring increases with pump intensity and strength of the nonlinearity. Of these two parameters we have control only over the pump intensity experimentally. It should be noted that the angles of the signal and idler beams satisfy equation 3.2 within the crystal. Upon exiting the crystal the beams refract which increases the angle. In what follows, we discuss the second order temporal coherence function to characterise our single-photon source. The experimental arrangements to prepare and characterise single excitation states are then detailed in the next section. The chapter closes with a discussion of the experimental results.

3.2.1 Characterisation

Generally, the second-order coherence function $g^{(2)}$ is a function of the time-delay τ between two measurements. At a fixed position it is a measure of the joint probability of detecting a photon at time t and another at some later time $t + \tau$. Equivalently for classical fields, it is a measure of the correlation between intensities. It can be measured at the two outputs of a beamsplitter, as in the Hanbury-Brown Twiss (HBT) intensity interferometer shown in Fig. 3.3b. Classically it is given by [28, 29]

$$g_{BB'}^{(2)}(\tau) = \frac{\langle I_B(t + \tau)I_{B'}(t) \rangle}{\langle I_B(t + \tau) \rangle \langle I_{B'}(t) \rangle} \quad (3.3)$$

where I_B and $I_{B'}$ are the intensities measured by detectors B and B' respectively. For a 50:50 beamsplitter Eq. 3.3 may be written in terms of the input intensity I , with $I_B(t) = I_{B'}(t) = I(t)/2$. Then at zero time-delay and after applying the Cauchy-Schwartz inequality, Eq. 3.3 becomes

$$g_{BB'}^{(2)}(0) = \frac{\langle [I(t)]^2 \rangle}{\langle I(t) \rangle^2} = g^{(2)}(0) \geq 1 \quad (3.4)$$

Thus $g^{(2)}(0)$ has a lower bound of 1 for classical light, while for photon-number states $g^{(2)}(0)$ takes the form [29]

$$g^{(2)}(0) = \frac{\langle \hat{n}(\hat{n}-1) \rangle}{\langle \hat{n} \rangle^2} = 1 - \frac{1}{n} \quad (3.5)$$

where \hat{n} is the photon-number operator and n is the mean photon number. In the case of single-photon states $n = 1$ and so $g^{(2)}(0) = 0$. For $n = 2$, $g^{(2)}(0) = 0.5$, and so experimentally for a single excitation we expect a value less than 0.5 and ideally close to zero. Equation 3.5 can be derived from $g^{(2)}(\tau) = \frac{\langle \hat{E}(t)\hat{E}(t+\tau)\hat{E}^\dagger(t+\tau)\hat{E}^\dagger(t) \rangle}{\langle \hat{E}(t)\hat{E}^\dagger(t) \rangle \langle \hat{E}(t+\tau)\hat{E}^\dagger(t+\tau) \rangle}$, where \hat{E} is the electric field operator and \hat{E}^\dagger is its Hermitian conjugate. Interestingly one arrives at the same τ -independent result for both a multi-mode and single-mode field [29].

In the context of the experiment, $g^{(2)}(\tau)$ for heralded single-photons can be expressed as [28]

$$g^{(2)}(\tau) = \frac{N_{ABB'}(\tau)N_A}{N_{AB}N_{B'}(\tau)} \quad (3.6)$$

where each factor is a count rate with a subscript indicating at which detector. Two or more subscript letters represents coincidence rates between the indicated detectors. Ideally $N_{ABB'}$ should be zero, however we find that this is not the case due to detector dark-counts, background light, and a non-zero down-conversion linewidth and coincidence window.

To measure the coincidence window τ_c , we consider $g^{(2)}(\tau)$ of unheralded photons using two detectors. In this case detections at detector A are disregarded, and $g^{(2)}(\tau)$ takes the form

$$g^{(2)}(\tau) = g_{2-det}^{(2)}(\tau) = \frac{N_{BB'}(\tau)}{N_B N_{B'}} \frac{T}{\tau_c} \quad (3.7)$$

where T is the integration time. Without heralding to post-select single-photon states from an otherwise classical state in the mode, this value must equal 1 for all τ . We may then average several $g_{2-det}^{(2)}(\tau)$ for N different τ values, then equate to 1 and solve for τ_c :

$$\tau_c = \frac{T}{N} \sum_i \frac{N_{BB'}(\tau_i)}{N_B(\tau_i)N_{B'}(\tau_i)}. \quad (3.8)$$

3.2.2 Experimental Setup

In the type 1 SPDC single-photon source shown in Fig. 3.3a, a 3 mm thick $\beta - BaB_2O_4$ (BBO) crystal is pumped with the 405 nm CW laser. A small percentage of pump photons undergo SPDC in the BBO crystal to produce photon-pairs with a half-opening angle $\sim 3^\circ$ and a central wavelength of 810 nm. The lens system (LS) collimates and focuses the pump beam onto the crystal, thus improving efficiency by increasing the power per unit area. The lenses (LC) on both of the down-conversion arms are placed a distance of one focal length away from the crystals centre to collimate them, thereby improving collection by the fibre-couplers (FC). Placed before each fibre-coupler is a single interference filter (IF). These filters select either a (800 ± 20) nm or (810 ± 5) nm wavelength band of down-converted photons, depending on the filter used. These photons are then coupled into single-mode fibres by the FCs which each consists of a 20x microscope objective and XYZ-translation stage. The smaller numerical aperture of these fibres acts to spatially select the centre of the down-conversion mode. This along with filtering results in better correlated photon-pairs (i.e. fewer triple coincidences $N_{ABB'}$). Since the down-converted photons are produced in pairs, a photon in arm 1 can be used to herald the arrival of a photon in arm 2. This effectively post-selects true single photons from an otherwise classical state.

To measure $g^{(2)}(\tau)$, a HBT intensity interferometer is used and is shown in Fig 3.3b. The single-mode (SM) fibre of arm 1 is connected to a multi-mode (MM) fibre through which heralding photons are decoupled and focused onto a single-photon avalanche diode detector (SPAD) (Excelitas SPCM-AQRH-15) denoted A. The single-mode fibre on arm 2 which is also polarisation-maintaining (PM) is similarly connected to a multi-mode fibre. The heralded photons from this fibre are subject to the HBT interferometer such that we may measure correlations between photo-detections at SPAD detectors B and B'. The signal from detector B' is sent to an electronic delay circuit. It allows us to introduce delays (τ) from 0.5 ns to 63.5 ns with a resolution of 0.5 ns. Extra lengths of cabling is used to delay the signals from detectors A and B making it possible to set negative time delays (B' arrives before A and B) using the delay circuit. The three signals are then sent

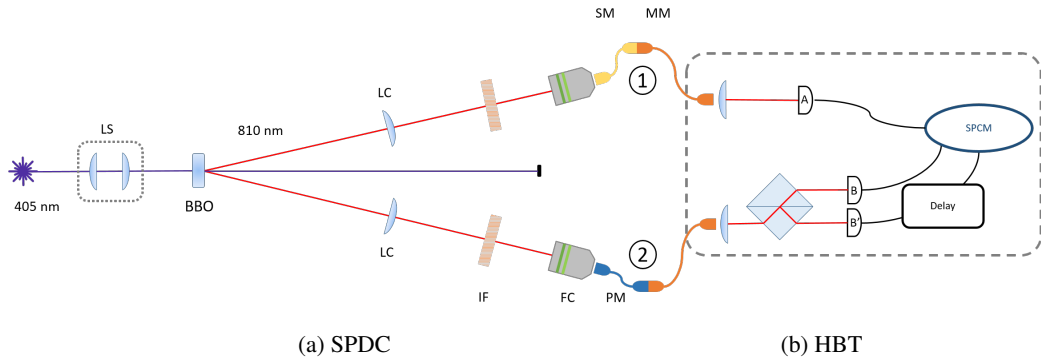


Figure 3.3: Single-photon source setup. It consists of (a) a spontaneous parametric down-conversion setup and (b) a Hanbury-Brown and Twiss interferometer with accompanying electronics (enclosed in dashed box) used for $g^{(2)}$ measurements.

to a single-photon counting module which then outputs the single-photon count rates at each detector and the coincidence rates between detectors to a PC. The coincidence rate is the number of detections in B and B' collectively that occur within $\sim 8 \text{ ns}$ (the chosen coincidence window) of a detection in A. The counts rates can be monitored in real-time or recorded and saved to a file using a LABVIEW program.

The measurement procedure was to record 10 sets of all count rates with an integration time of 10 s for τ values from -8.5 ns to 8.5 ns in steps of 0.5 ns . This was done for two interference filter combinations: the narrow 810 nm filter on both arms and then with the wider 800 nm filter on arm 2. Using the narrower filters produces better correlated photon-pairs at the cost of lower count rates. This is not ideal when trying to excite single-SPPs; a process which incurs great loss due to supporting optics, inefficiency of coupling schemes, and exponential decay. To mitigate these effects a larger input count rate is desirable, and it is achieved here by using the wider 800 nm filter on arm 2 of the source. It is the heralded photons of arm 2 that is later used to excite single-SPPs.

3.2.3 Results and Discussion

As an indication of performance, typical count rates achieved at $\tau = 0$ with both filter combinations are shown in Tab. 3.1. The 800 nm filter greatly increases the single count rates of B and B' but does not significantly affect the coincidence rates - at most a 3000 cps difference has been observed. At the time of measurement the difference was two orders magnitude lower than the coincidence rates themselves. Increasing the single rates while maintaining the coincidences results in a larger triple coincidence rate. As such, a larger $g^{(2)}(0)$ is then expected.

Filter	$N_A(10^3 \text{ cps})$	$N_B(10^3 \text{ cps})$	$N_{B'}(10^3 \text{ cps})$	$N_{AB}(10^2 \text{ cps})$	$N_{AB'}(10^2 \text{ cps})$	$N_{ABB'}(10^2 \text{ cps})$
810nm	260	120	140	48	58	0.1
800nm	240	290	350	48	58	0.2

Table 3.1: Count rates produced by single-photon source.

For each recorded set of count rates a $g^{(2)}$ value was calculated using Eq. 3.6. The average and standard deviation of sets of $g^{(2)}$ values for each τ was then calculated to obtain the $g^{(2)}(\tau)$ plots presented in Fig. 3.4a and 3.5a. The average values of $g^{(2)}(0)$ were (0.096 ± 0.009) and (0.160 ± 0.008) for the 810 nm and 800 nm filters respectively. Both values violate the classical lower-bound of 1 and are less than 0.5, thus indicating single excitations. The wider filter produced a larger $g^{(2)}(0)$ as expected.

A note on the shape of the experimental $g^{(2)}(\tau)$: Eq. 3.5 predicts a constant value of zero for all τ , but it does not consider the effect of the heralding. However, Eq. 3.6 which was used to obtain these plots does include heralding effects. According to Ref. [30], there is a strong correlation between detections at A and B' which dominate the form of Eq. 3.6. Assuming our photons have a Gaussian temporal wavepacket, then the correlation between photon detections at A and B' ($N_{AB'}$) is Gaussian as well. Thus Eq. 3.6 takes the form of

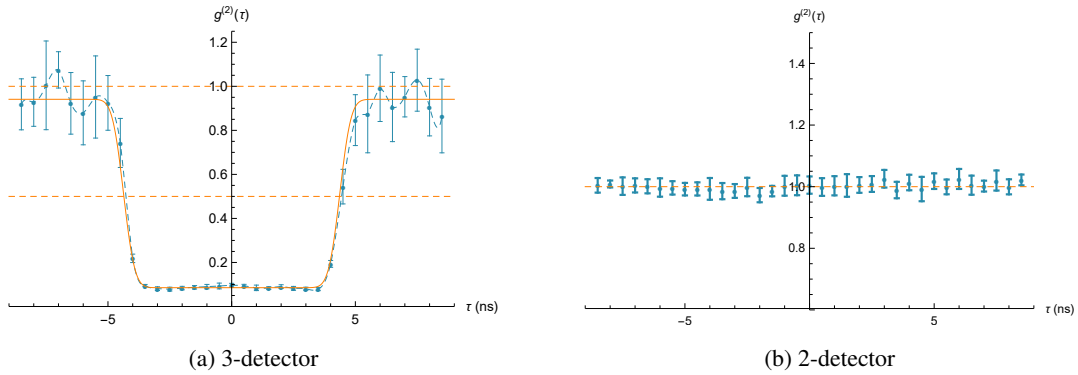


Figure 3.4: Second-order coherence coefficient against time delay of heralded photons filtered by an 810nm IF.

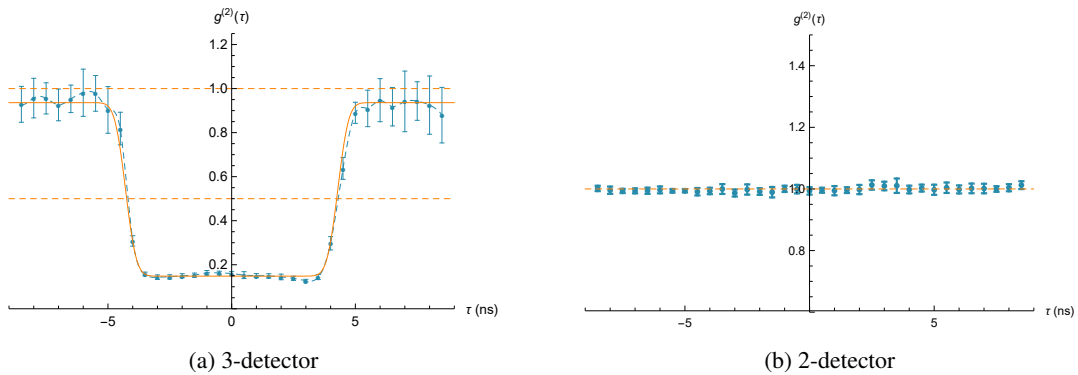


Figure 3.5: Second-order coherence function against time delay of heralded photons filtered by an 800nm IF.

a Gaussian well, the width of which is equal to the coherence time. Since the coincidence window at $\sim 8\text{ ns}$ is much larger than the sub-picosecond coherence time, we have a broadening of the well. This process can be modelled as a convolution of a τ_c -wide top-hat function with the Gaussian shaped $N_{AB'}$ [30], which can be shown to have the form: $\text{erf}(\tau - w) + \text{erf}(-\tau - w)$. Here $\text{erf}(z) = \frac{2}{\sqrt{\pi}} \int_0^z e^{-t^2} dt$ is the error function, and w is the width of the plateau consisting of the coincidence window, coherence time, and detector jitter time.

By fitting a function of the form $f(\tau) + f(-\tau)$ where $f(\tau) = a\text{erf}(b\tau + c) + d$ we can extract parameter c as the base-width of the well and thus estimate $\tau_c \approx c$. Doing so yielded values of $(9 \pm 1)\text{ ns}$ and $(8.8 \pm 0.8)\text{ ns}$ for the $810\text{ nm}/810\text{ nm}$ and $810\text{ nm}/800\text{ nm}$ filter combinations respectively. These values include the coherence time of the photons and jitter time of the detectors. A better method employed was to use Eq. 3.8 to calculate values of τ_c in the same manner as was done for $g^{(2)}(\tau)$. Taking the average of these values gave $\tau_c = (8.3 \pm 0.1)\text{ ns}$ and $\tau_c = (8.28 \pm 0.05)\text{ ns}$ for the $810\text{ nm}/810\text{ nm}$ and $810\text{ nm}/800\text{ nm}$ filter combinations respectively. Then using the grand mean of $\tau_c = (8.29 \pm 0.15)\text{ ns}$ and Eq. 3.7 on the data we obtain plots of $g_{2-\text{det}}^{(2)}(\tau)$ shown 3.4b and 3.5b.

Chapter 4

Stripe Waveguides: Simulations

Before experimentally probing plasmonic stripe waveguides, a series of simulations were run. The purpose of which was to determine the best grating period for excitation by single-photons and the red alignment laser. Beyond this, it also provided insight which proved useful in the lab. The frequency domain simulations described in this chapter were built using the finite element method in COMSOL - a commercial multiphysics modelling application. The finite element method is a numerical technique in which the computational domain is discretized to form a mesh. The solution to Maxwell's equations can then be approximated using interpolating functions [49].

We simulate a two-dimensional geometry as shown in Fig 4.1. It consists of a flat waveguide with a rectangular-profile input grating. The structure rests on a silica substrate and is exposed to air (vacuum). These elements are padded above and below by $1 \mu m$ wide perfectly matched layers (PML) which are regions of an artificial absorptive material. This coupled with the scattering boundary condition (BC) applied to the outer boundaries emulates an unbounded domain. The scattering BC prevents light incident on the boundary from reflecting back into the domain. It is one of several predefined boundary conditions in COMSOL. Another BC used in all simulations to follow is the port BC. It is applied on the air-PML interface, and is used to excite fields in the domain. For simulations involving an input grating, it is set to excite a Gaussian beam with a $2 \mu m$ width centred and focused on the grating. Several port BCs may be used in conjunction to extract transmission and reflection plots, but this feature is not used here. Instead, to calculate the transmission, the time averaged power flow of the SPPs is integrated along a line in the SPP field which is two grating periods into the waveguide section. The line is shown in red and is labelled "Probe" in Fig. 4.1). The input power is set at $1 W$ so that the transmission values calculated do not need normalising.

An optimisation of the input grating is presented below, followed by a demonstration of the characteristics to be measured experimentally. Lastly, we look at the effect of varying output grating parameters.

4.1 Grating Optimisation

To optimise the input grating, its geometry was parameterised by the three variables p , h and $dc = \frac{u}{d}$ as indicated in Fig. 4.1. These variables are the grating *period*, *height*, and *duty-cycle* (DC) respectively. The procedure was to fix one parameter and then simulate SPP excitation for combinations of the remaining two. Transmissions plots are then extracted from the resulting simulations. In this manner a dual period-height and period-DC optimisation was carried out for input wavelengths of $\lambda = 780\text{ nm}$ and $\lambda = 810\text{ nm}$. When fixing the height and duty-cycle, the values used were 90 nm and 0.5 . These parameter values, along with the thickness $t = 70\text{ nm}$, were those of the available fabricated waveguides. These values were suggested by previous work [35]. The maximum mesh element size used was $\lambda/5$. Lastly, the dielectric function used for gold was that of Johnson and Christy [41] unless otherwise stated.

4.1.1 Period and Height Optimisation

The duty-cycle was fixed at 0.5 while the grating period and height were both varied in steps of 10 nm . The period ranged from 620 nm to 820 nm and the height from 10 nm to 90 nm . Each combination of period and height was simulated and SPP transmission coefficients extracted. The graphs in Fig. 4.2 were constructed using these transmission coefficients.

Figures 4.2a and 4.2c show transmission as a function of period for different grating heights. From these graphs the optimal period-height combination is $(p = 710, h = 60)\text{ nm}$ for $\lambda = 780\text{ nm}$, and $(p = 740, h = 60)\text{ nm}$ for $\lambda = 810\text{ nm}$. The optimal periods were expected to be equal to the SPP wavelengths of $\sim 760\text{ nm}$ and $\sim 790\text{ nm}$ corresponding to freespace input wavelengths of 780 nm and 810 nm . In both cases the optimal period is smaller than the expected. The adjacent figures 4.2b and 4.2d are discrete surface plots of transmission against period and height. Figs. 4.2a and 4.2b are for $\lambda = 780\text{ nm}$, while 4.2a and 4.2d are for

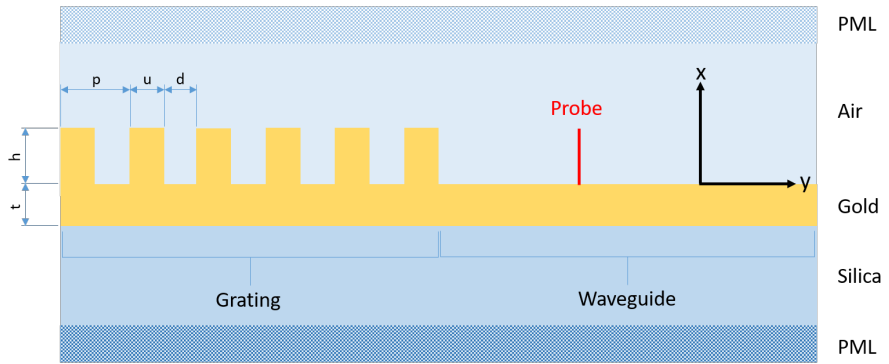


Figure 4.1: Waveguide geometry showing parameters considered for optimisation. The coordinate system is chosen differently to that introduced in the theory of Chapter 2 due to convenience in design when using COMSOL.

$\lambda = 810 \text{ nm}$. These plots have two maxima which do not change significantly with the period. The global maximum is the optimal parameter combination described above. The secondary maximum for a 780 nm input is ($h = 70, p = 785$) nm and ($h = 80, p = 810$) nm for an 810 nm input. These are closer to the expected but slightly too large. The deviation of the periods from the expected is due to the high grating. Each grating element acts as an antenna on which localised fields may be excited. This causes distortions in the SPP dispersion relation which become more prevalent at greater height (depths) [1, 44].

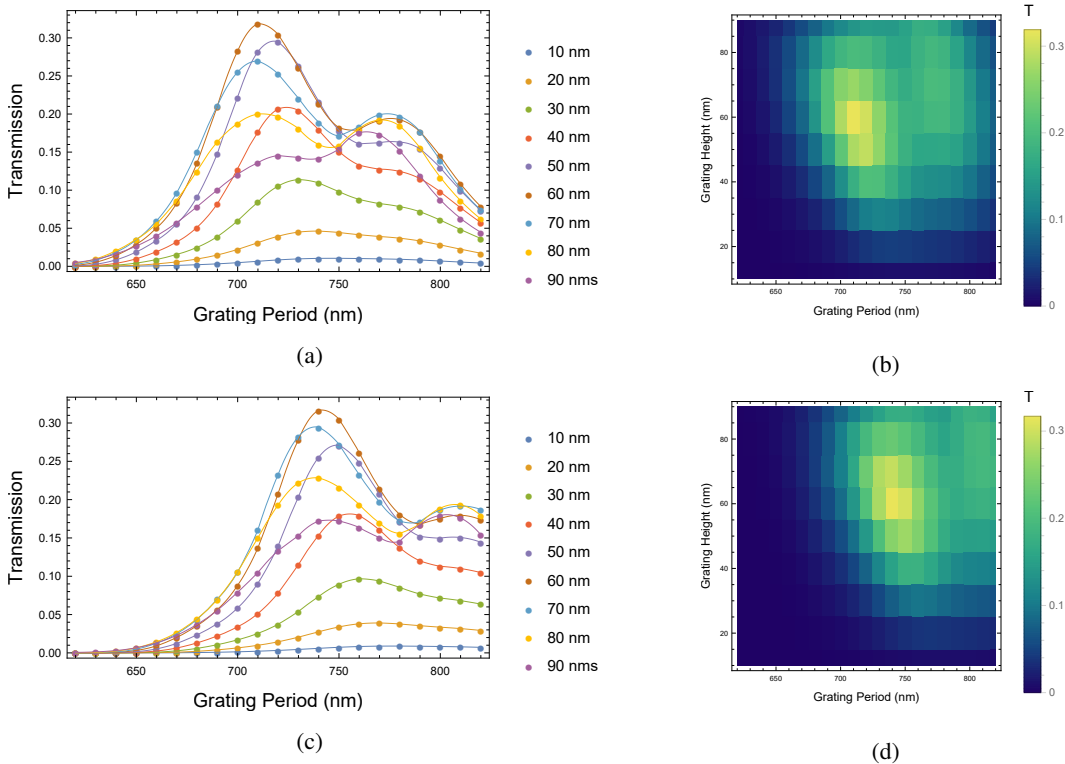


Figure 4.2: Period-Height Sweep. The graphs show the simulated SPP transmission against grating height and period combinations. In (a) and (c) each curve represents a fixed grating height, while (b) and (d) show the corresponding discrete density plots.

4.1.2 Period and Duty-cycle Optimisation

The period-DC optimisation followed the same procedure as that of the period-height. The height was now fixed at the 90 nm and the duty-cycle was varied from 0.1 to 0.9 in steps 0.1. The results are illustrated in the transmission plots in Fig. 4.3. Figures 4.3a and 4.3c indicate that the dc values between 0.4 and 0.5 are most suitable for both input wavelengths. Moving away from these values we have longer flat regions between scatterers, thus making the grating more mirror-like and much less effective. This is clearer in the surface plots (Figs. 4.3b and 4.3d). Also notable is that varying dc shifts the maxima. Again this is due to the antenna-like behaviour of the grating elements. This time the effect is more significant as we are actively

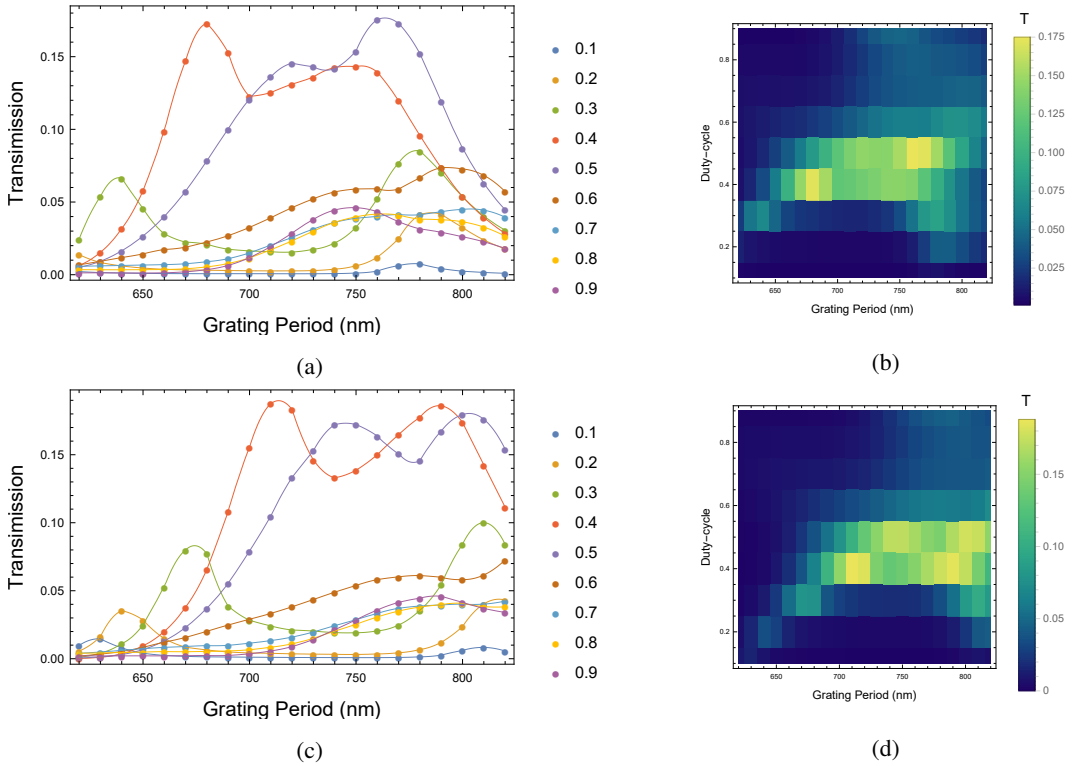


Figure 4.3: Period-DC Sweep. The graphs show the simulated SPP transmission against grating duty-cycle and period combinations. In (a) and (c) each curve represents a fixed dc value, while (b) and (d) show the corresponding discrete density plots.

varying the antennae length.

4.2 Characterisation

Having established the appropriate parameters for SPP excitation at the wavelengths of interest, simulations were then ran to demonstrate measurable SPP characteristics. This served to test the reliability of the simulations, as well as provide a benchmark for experimental results. At the time, with the available resources, the measurable characteristics were the polarisation dependence of in-coupling, and the exponential intensity decay. The general geometry was the same as that depicted in Fig. 4.1. For the polarisation test the parameters were $t = 70 \text{ nm}$, $h = 90 \text{ nm}$ and $dc = 0.5$ for both wavelengths. These values were used such that the simulation may more closely resemble the experiment. The periods used were $p = 700 \text{ nm}$ and $p = 740 \text{ nm}$ for $\lambda = 780 \text{ nm}$ and $\lambda = 810 \text{ nm}$ respectively. These were the available periods closest to the optimal values ascertained in the previous section. In the case of the decay length simulations, the optimal periods were used instead. This was to ensure higher intensity at larger distances.

4.2.1 Polarisation Dependence

Consider that the waveguide rests on the yz plane and parallel to the y axis as shown in Fig. 4.1. Assuming a field normally incident on the grating, we may write its electric field as $\vec{E} = E_0(0, \cos(\theta), \sin(\theta))$. Since the transverse (z) component cannot couple into the SPP mode, we have that $E_{SPP} \propto E_0 \cos(\theta) \implies I_{SPP} \propto E_0^2 \cos^2(\theta)$. Thus the transmission against polarisation angle should display a $\cos^2(\theta)$ form. Simulating SPP excitation for θ varied from 0° to 180° in steps of 5° yielded the plots in Fig. 4.4. Curves of the form $a \cos^2(b\theta)$ were fitted to the simulated results. The correlation coefficient r^2 of the fittings for $(\lambda = 780\text{nm}, p = 700\text{nm})$ and $(\lambda = 810\text{nm}, p = 740\text{nm})$ were 0.99998 and 0.99996 respectively. r^2 is a measure of how close the least squares fitting is to the original data, and takes values between 0 and 1. A value of 1 indicates a perfect fit, while 0 indicates the opposite extreme. The fit parameters are given in Tab. 4.1. The results clearly exhibit the expected $\cos^2(\theta)$ behaviour.

Wavelength (nm)	Period (nm)	a ($\times 10^{-4}$ a.u.)	b
780	700	477.2 ± 0.4	1.0003 ± 0.0004
810	740	752.6 ± 0.8	1.0006 ± 0.0006

Table 4.1: Fit parameters for simulated polarisation dependence plots in figure 4.4.

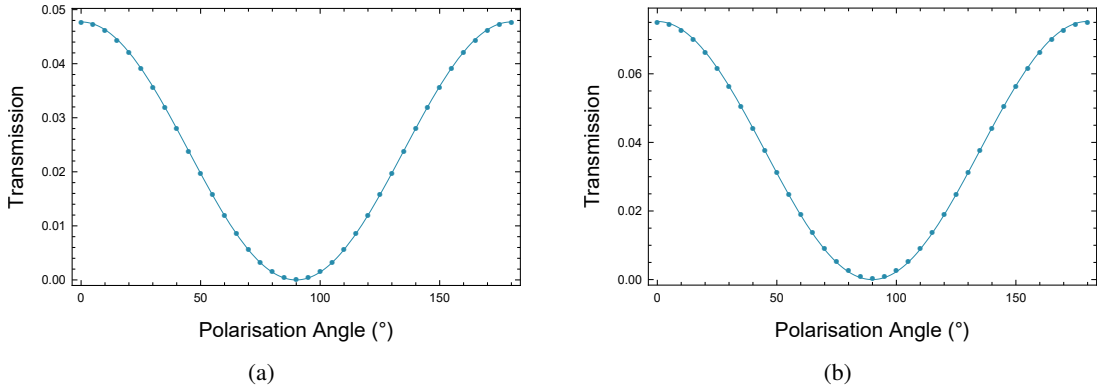


Figure 4.4: Simulated demonstration of the polarisation dependence of in-coupling (TM mode restriction of SPPs). (a) Input wavelength $\lambda = 780\text{ nm}$ and (b) $\lambda = 810\text{ nm}$.

4.2.2 Decay Length

In these simulations, the waveguide section was extended to $30\text{ }\mu\text{m}$. This was to ensure a sufficiently long distance over which we could extract SPP intensities. In hindsight, a distance $> 50\text{ }\mu\text{m}$ would have been more appropriate (but not necessary). Along the air exposed surface of the waveguides, 29 probe lines were placed $1\text{ }\mu\text{m}$ apart. The first of these was a distance of two periods away from the grating. Calculating the transmission through these lines and dividing by the maximum, we obtain a plot of normalised transmission against propagation distance. An exponential curve, $e^{-\frac{x}{L}}$, was then fitted in order to determine the decay

length L . The amplitude was set to 1. Since the theory describes an infinite half-space while experimentally we probe waveguides of finite thickness t , it is sensible to consider the effect of t on L . To do this, decay curves for waveguides with t values varied from 50 nm to 90 nm in steps of 10 nm were simulated. This was done for $\lambda = 780 \text{ nm}$ and $\lambda = 810 \text{ nm}$ and using dielectric constants for gold from and Johnson & Christy [41], and Rakić *et. al.* [42] (which tends to be more lossy). Figure 4.5 shows the simulated decay curves for $\lambda = 810 \text{ nm}$. Table 4.2 summarises the fit parameters for both input wavelengths. The exponential form fits well to the points giving r^2 values above 0.9998. On closer inspection there is a small deviation at shorter propagation distances. This deviation is present until $\lesssim 10 \mu\text{m}$ for $t = 90 \text{ nm}$, and is less prevalent with decreasing t . This is because the SPP does not develop immediately after the grating with the characteristic intensity profile. The results show that as t increases, L approaches the theoretical value for an infinite half-space. It is also noted that the complex dielectric constants from Johnson is consistently less lossy (smaller imaginary part) than that obtained from Rakić. It would be expected that the experimentally determined decay lengths of bound SPPs should be between or close to those L values obtained for $t = 70 \text{ nm}$.

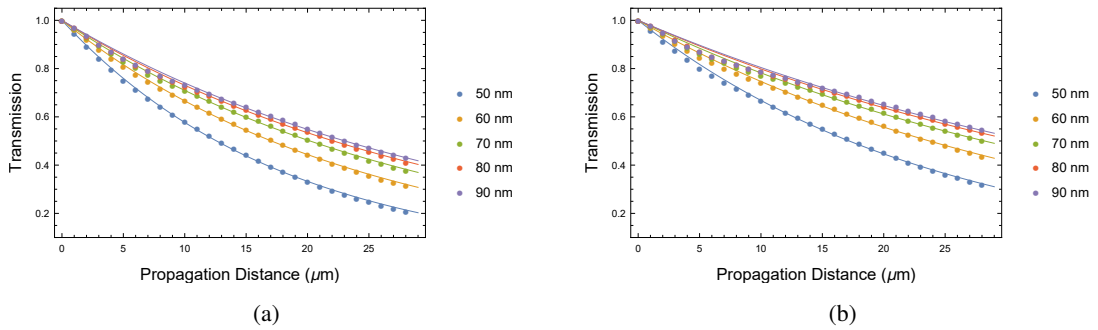


Figure 4.5: Simulated decay of SPP intensity in direction of propagation for varied waveguide thickness. The graphs (a) and (b) are obtained using dielectric functions of Rakić *et. al.* and Johnson & Christy respectively.

$t \text{ (nm)}$	810 nm		810 nm		780 nm		780 nm	
	$L \text{ (\mu m)}$							
50	20.68 ± 0.05	15.198 ± 0.003	24.8 ± 0.1	18.17 ± 0.05				
60	28.66 ± 0.09	20.61 ± 0.04	34.2 ± 0.2	24.61 ± 0.08				
70	34.46 ± 0.15	24.59 ± 0.06	40.7 ± 0.3	29.1 ± 0.1				
80	38.03 ± 0.21	27.13 ± 0.07	44.4 ± 0.4	31.9 ± 0.2				
90	39.80 ± 0.29	28.47 ± 0.11	46.0 ± 0.5	33.3 ± 0.2				

Table 4.2: Simulated decay lengths L of waveguides with varied thickness t . Dielectric constants from Johnson were used for columns 2 and 4. Constants from Rakić were used for columns 3 and 5. The goodness of fit measure r^2 were greater than 0.999 for all fitted curves.

4.2.3 Spectral Response

The simulations thus far employed monochromatic light for SPP excitation. Experimentally this is not the case; the light from the single-photon source and alignment laser have widths on the order of tens of nanome-

ters. The width and peak wavelengths of the input gratings spectral response needs to be known, as these will distort the output spectrum. If the width of the response is smaller than that of the input spectrum, the output spectrum will be narrower than the input. This will mean a lower output power. In the case of single-photon input this is beneficial, provided that the dominant wavelength of the response corresponds to the central down-conversion wavelength. If this is not so, the peak wavelength of the output spectrum will shift. Thus increasing the $g^2(0)$ value by decreasing the N_{AB} and $N_{AB'}$ coincidence rates.

The spectral response of fabricated gratings with parameter sets ($p = 700 \text{ nm}, h = 90 \text{ nm}, dc = 0.5$) and ($p = 740 \text{ nm}, h = 90 \text{ nm}, dc = 0.5$) were simulated. The resulting graphs are shown in Fig. 4.6. The plots for $p = 740 \text{ nm}$ have peaks at the appropriate wavelength 810 nm , while the $p = 700 \text{ nm}$ plots do not have peaks at 780 nm . This is due to the period being smaller than the simulated optimal value of 710 nm . This will not be an issue experimentally, as the responses are comfortably broad compared to the spectra of the input light. Thus these gratings appear suitable for the input wavelengths of interest. Also of note here is the double-peak feature. The lower wavelength peaks at $\sim 760 \text{ nm}$ and $\sim 730 \text{ nm}$ correspond to SPP wavelengths of $\sim 740 \text{ nm}$ and $\sim 710 \text{ nm}$ respectively.

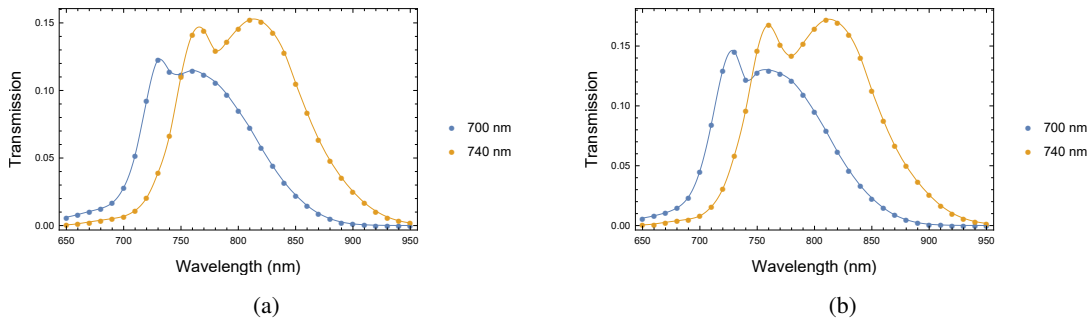


Figure 4.6: Simulated spectral response of input gratings. Each curve represents the response of a grating with a period specified in the legend. Figure (a) and (b) made use of dielectric constant from Rakić *et. al.* and Johnson & Christy respectively.

4.3 Out-coupling Simulations

Gratings like those used for in-coupling can be used to decouple light from the SPP mode. Some light may be scattered out while some may remain having been either transmitted to the other side of the grating or reflected backwards. The ideal output grating would minimize the transmitted and reflected SPP intensities, thereby maximising the photonic output. In this section we investigate the effect of the grating parameters on these three modes via simulation. The geometry used is shown in Fig. 4.7. On either side of the grating are flat waveguide sections. A port boundary, positioned $2.5 \mu\text{m}$ away from the left edge of the grating, was used to excite SPPs using the end-firing method. Out-coupling was simulated for an input wavelength of 810 nm , and with one of three parameters varied while the other two remained fixed. Transmission coefficients were

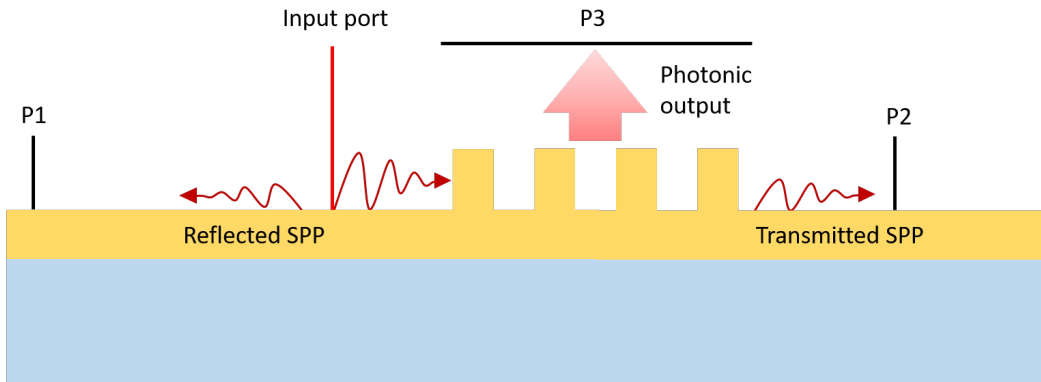


Figure 4.7: Geometry of out-coupling simulations. Lines P1, P2, and P3 are the probe lines along which the transmission was calculated for the reflected and transmitted SPPs, and the photonic output respectively.

then calculated for the photonic output, as well as the reflected and transmitted SPPs. The resulting plots are shown in Fig. 4.8. From these plots we see that there is no single optimal period; values between 620 nm and 730 nm are all sufficient. The optimal height and duty-cycle are 55 nm and 0.5 respectively.

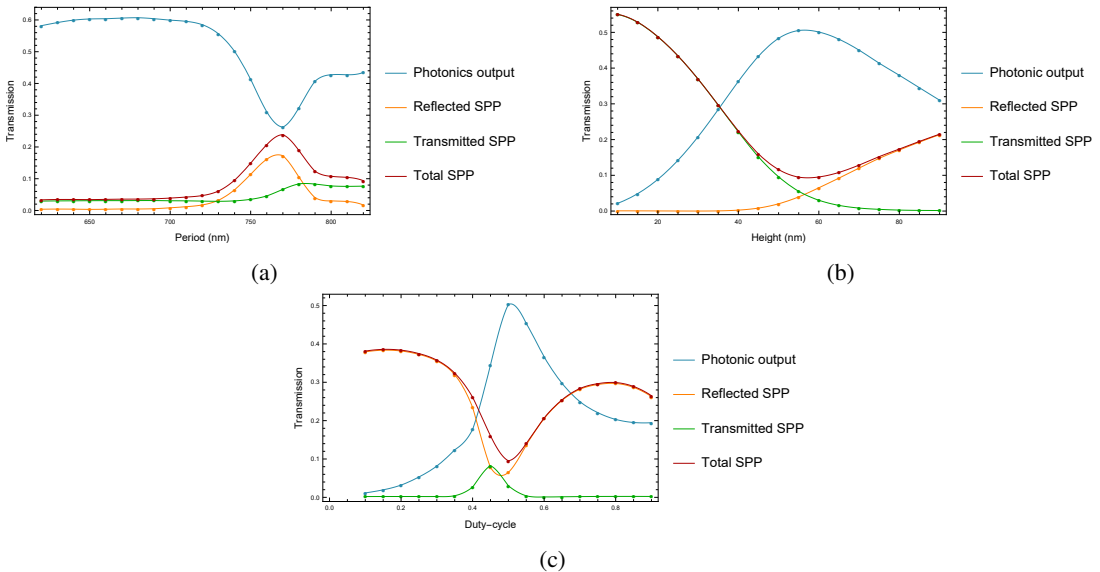


Figure 4.8: Plots of out-coupled light and SPP transmission as a function of (a) period, (b) grating height, and (c) duty-cycle. (a) As the length of the grating elements approach $\sim \frac{\lambda_{SPP}}{2}$ a resonance dip develops. Beyond the dip, the graph plateaus at a lower efficiency due to the longer flat sections at higher periods. This allows the SPP to traverse the grating. Smaller periods scatter light out more rapidly, producing a more narrow and intense beam. (b) The grating becomes more reflective and less transmissive as the height increases. The optimal height for out-coupling lies at the intersection of the SPP transmission and reflection curves.

Chapter 5

Stripe Waveguides: Experiments

On route to confirming the photon-number preserving nature of SPPs, the experimental capability to excite them must first be developed. In this chapter, the experimental setup built to achieve this in the classical and quantum regimes is detailed. Confirmation of SPP excitation is carried out by demonstrating two characteristic behaviours of SPPs in the classical and quantum regimes. The first of these is the polarisation dependence of photon to SPP coupling due to the TM mode restriction. The second is the exponential decay of SPP intensity with propagation distance. An additional characteristic is the evanescent confinement at the metal-dielectric interface. Using near-field scanning techniques the fields intensity profile may be mapped and the decay length extracted. This measurement was not viable during the tenure of this work.

The structures probed were gold stripes $2 \mu\text{m}$ wide and 70 nm thick with a 90 nm high surface-relief diffraction grating at either end. They were fabricated in a two-stage electron-beam lithography and gold evaporation process onto a silica substrate. The first stage applies the flat waveguides onto the substrate while the second stage applies the gratings. A range of waveguide lengths and grating periods were fabricated. In Fig. 5.1 is an atomic force microscope (AFM) (NT-MDT NTEGRA Prima) image showing a sample of the fabricated waveguides, along with a 3D rendering of the general structure.

5.1 Experimental Setup

The microscope setup used to probe the plasmonic waveguides is shown in Fig. 5.2. The most important constituent is the diffraction-limited microscope objective (100x DLM) which allows us to adequately image the waveguides on the CCD camera, as well as focus the input beam to a spot size of roughly $2 \mu\text{m}$. The waveguides are illuminated by a bright LED, the light from which is condensed using a 10x microscope objective. The image is directed onto the camera by the beamsplitter (BS) and a mirror. The plasmonic

chip containing a range of waveguides is mounted on a Thorlabs NanoMax XYZ translation stage to allow positioning. Using this stage, the image is focused onto the camera by adjusting the distance between the chip and 100x objective. Changing the focus in this manner also changes the input beam spot size on the chip. The spot size is adjusted by shifting the lenses on the input beam. This ensures that the image is focused and the beam spot is $\sim 2 \mu\text{m}$ on the camera.

The input beam is injected via a PM fibre connected to a beam-collimator (BC). To excite SPPs, the input grating of the chosen waveguide is positioned at the beam spot. Light can then be seen at the output grating when using the alignment laser, as can be seen in Fig. 5.3. A linear polariser is used to remove any elliptical character from the input, while the first half-wave plate can be used to maximise throughput. The third half-wave plate is used to rotate the polarization such that it is parallel to the SPP propagation direction to maximise the coupling. For more efficient measurements the beamsplitter is flipped out of the beam path and a knife-edged mirror (KM) is used to pick off the output. The flip-mirror FM is then used to direct the output to the camera. Slight adjustments are made to the waveguide position to account for the small path deviation that was introduced by the BS. FM is then flipped out of the output beam path. The output light is then collected by a fibre-coupler (FC). The FC has three translation axes, and uses a 20x microscope objective to couple light into a multi-mode (MM) fibre. This fibre may then lead to a SPAD detector or spectrometer. Figure 5.3 shows an optical image of a waveguide in which the input ($\lambda = 780 \text{ nm}$) and output beams are visible. The resolution of the image does not allow us to discern the period of these gratings which are 700nm . A nanometer-resolution AFM image of a selection of longer waveguides with the same period is shown in Fig. 5.4. It is accompanied by a height-profile of the grating.

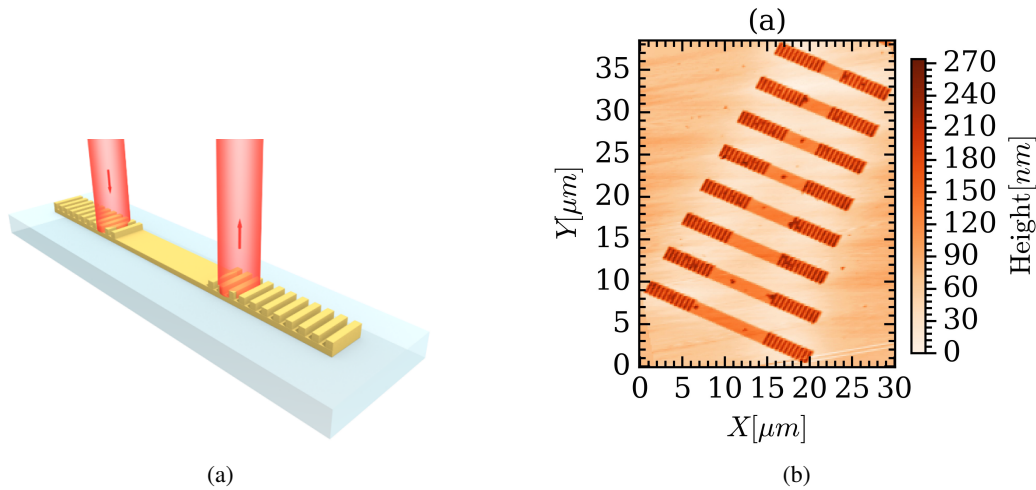


Figure 5.1: Waveguide structure. 5.1a a 3D image showing the waveguide with input and output gratings. 5.1b an AFM image of a few waveguides.

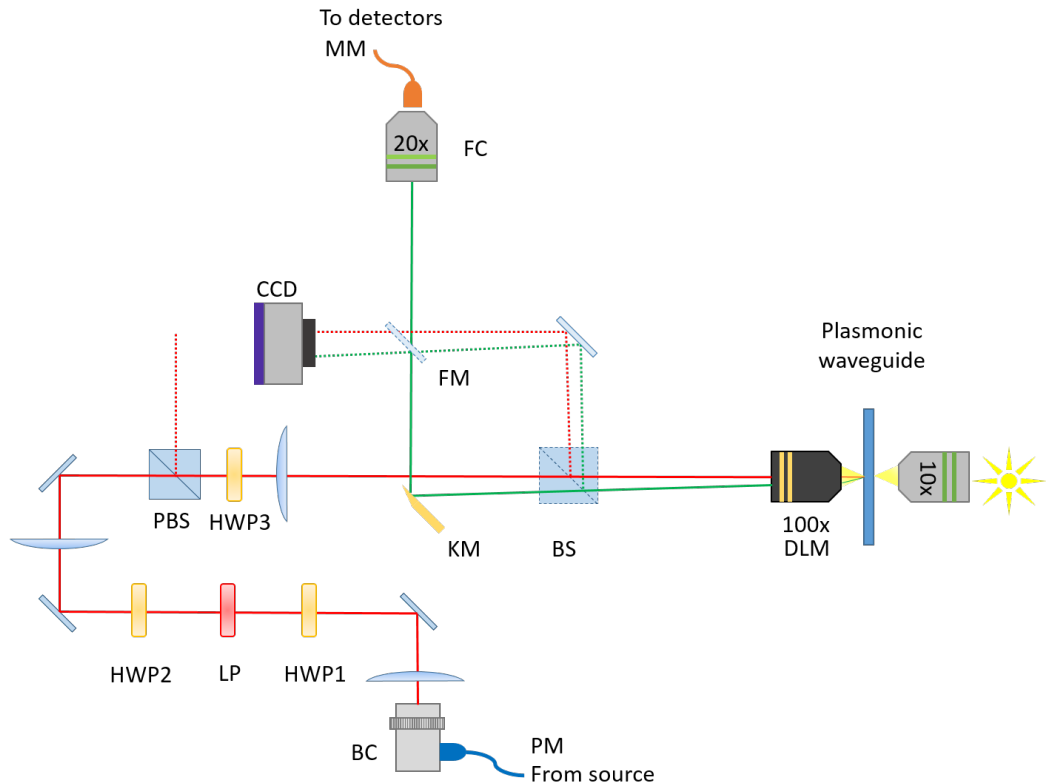


Figure 5.2: Compound Microscope stage used to probe plasmonic waveguides.

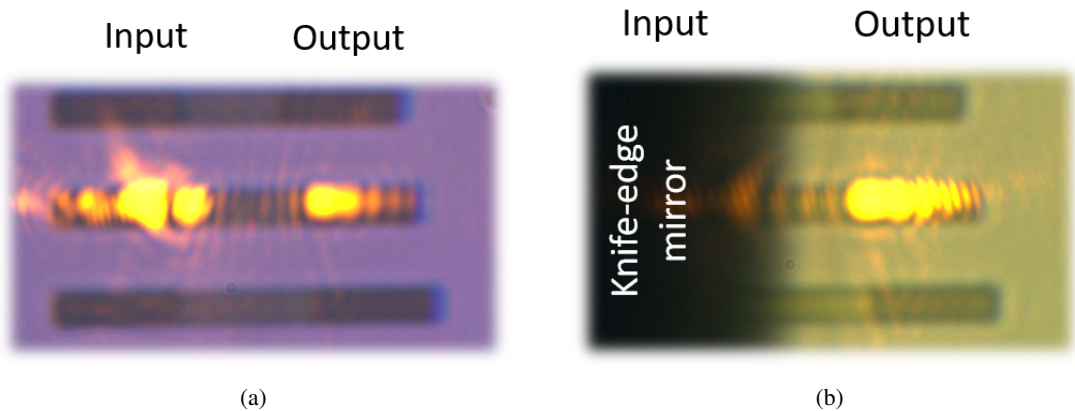


Figure 5.3: Optical image of waveguide obtained using the microscope stage. The gratings are distinguishable only as darker regions at each end of the waveguide. The reflection of input light can be seen above the left grating, while output light can be seen to the right. 5.3b. The image of the output grating and light picked-off by the knife-edge mirror KM.

5.2 Characterisation

With the capability to couple light into and out of waveguides provided by the probing setup of Fig. 5.2, the next step was to verify that SPPs were in fact excited. This is done by demonstrating the SPP characteristics.

In this section the experimental procedure followed to achieve this is detailed. It begins with a description of the polarisation-dependence measurement procedure in the classical and quantum regimes. This is followed by a measurement of the decay lengths, also in both regimes. Finally the determination of $g^{(2)}(0)$ of light decoupled from a waveguide is outlined.

A general alignment routine is followed before every measurement and is as follows. The beamsplitter BS is flipped into the beam path. Mirror FM is flipped down. The 780 nm alignment laser is then connected to the beam collimator. At this point the image of the waveguides and the input beam spot is visible using the camera. Half-wave plates HWP1 and HWP2 are adjusted to maximise throughput. This visibly increases the intensity of the beam spot. The chip is then positioned such that the input is on a grating. Light coupled to the waveguide is maximised using HWP3. Adjustments to the position are then made to increase the decoupled light intensity. BS is then flipped down and FM is flipped up. Only the output of the waveguide selected by KM is then viewable via the camera and by eye. Adjustments to the position are made once more, and then FM is flipped down. The output light is collected by the fibre-coupler FC. The spectrometer is connected to the FC and displays the spectrum of the output light on a monitor. The FC is optimised by translating along three axes to maximise the spectrum. The half-wave plates, mirrors, and chip position are then all fine-tuned to further optimise the coupling into the SPP mode and collection of the decoupled light.

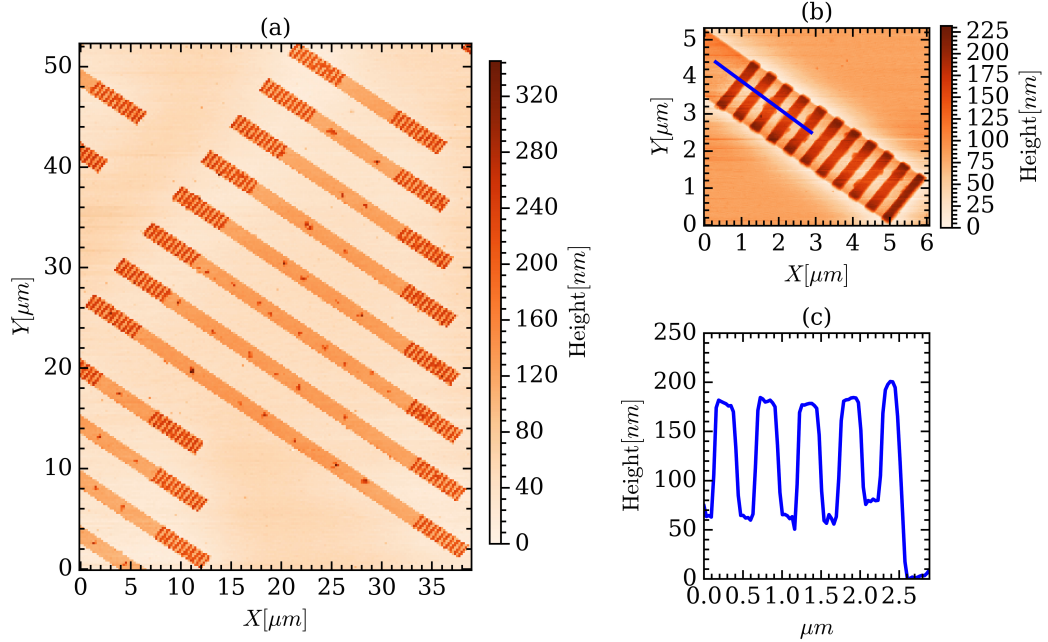


Figure 5.4: AFM image of longer waveguides used in classical measurements ($period = 700nm$). (a) Top view. (b) Higher-resolution of a grating only. (c) Height-profile of the grating in (b) along the blue line.

5.2.1 Classical

The classical measurements employed the 780 nm alignment laser for excitation, and the waveguides depicted in Fig. 5.4. Their lengths, L , range from $8.31\text{ }\mu\text{m}$ to $43.31\text{ }\mu\text{m}$ in steps of $5\text{ }\mu\text{m}$. These are the lengths of the actual waveguide section between the input and output grating.

Polarisation dependence: The aim here is to recover the expected \cos^2 behaviour of the relationship between the polarisation angle and SPP intensity. The out-coupled light intensity is directly proportional to the SPP intensity, and is also easily measured. Thus measurements of output intensity as a function of the polarisation angle θ were made. For this experiment, the shortest waveguide ($8.31\text{ }\mu\text{m}$) is used. The system is first aligned and optimised for this particular waveguide as described earlier. Once this is done, the spectrometer connected to the FC is replaced by a single-photon detector. The use of these detectors required that the input beam at 0.17 mW be attenuated. The polarising beamsplitter (PBS) with HWP2, and a variable ND filter inserted after the PBS was used for this purpose. After sufficiently attenuating the input, the halfwave plate angle was varied and the corresponding count rates were recorded using a LabView program. Ten measurements with a 1 s integration time for each waveplate angle was taken. After processing the data, the plot in Fig. 5.7a was obtained. Details on the data processing and analysis are discussed later.

Decay length: To obtain the decay curve (Fig. 5.7b) from which the decay length can be extracted, the out-coupled light intensity of the entire set of eight waveguides were measured. The input power was set at a higher power of 1.6 mW to ensure that the output of the longest waveguide was measurable. At this power it was feared that the SPAD detectors may saturate even with attenuation. Thus a power meter (ThorLabs, SI30VC) with console (ThorLabs, PM100D) was used. The out-coupled light power was measured 100 times over a 5 s period for each waveguide length L .

Spectral response: After the these measurements were carried out, the spectral response of the $p = 700\text{ nm}$ grating was approximated. A broad spectrum input (Fig. 5.5a) was injected into the probing setup and used to excite SPPs. The output light of the waveguide was collected and its spectrum measured (Fig. 5.5b). These spectra were rescaled such that the peak value was 1. The output spectrum is a distortion of the spectral response due to the non-uniformity of the input spectrum. To account for this, the output spectrum was rescaled by dividing it by the input spectrum. The result is the coupled response of both the input and output gratings (Fig. 5.5c). Additionally, due to the wavelength dependence of the output angle, the fibre coupler FC will not collect all wavelengths with equal efficiencies. Thus the spectrum will be distorted further. As a consequence of these issues, the response experimentally obtained cannot be compared to the simulated response. Nonetheless, it is insightful as it confirms that the overall spectral response covers the 780 nm input.

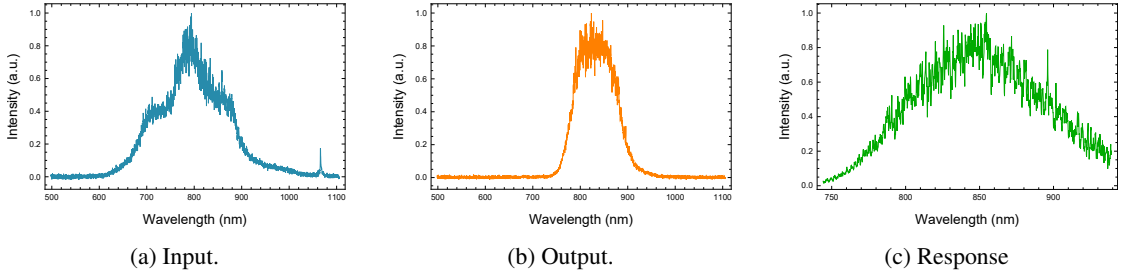


Figure 5.5: Spectral characterisation of a $p = 700\text{ nm}$ grating. 5.5a Spectrum of input light from white laser. 5.5b Output spectrum from waveguide. 5.5c Spectral response of input-output grating combination.

5.2.2 Quantum

The chosen grating period was 740 nm as suggested by the simulations. A smaller period of 700 nm was tested but found to be less efficient. An attempt at using a $p = 780\text{ nm}$ grating made alignment difficult as the visible component of the laser was poorly coupled into the SPP mode. To probe a selected waveguide in the quantum regime, the probing setup was aligned and optimised using the 780 nm laser following the general procedure described earlier. Once done, heralded photons from the single-photon source are injected into the system via the beam collimator. This arm of the source was filtered with a $(800 \pm 20)\text{ nm}$ interference filter. The output light of the waveguide was collected and sent to the HBT setup in Fig. 3.3b. Immediately, around 2000 counts per second were registered from B and B' collectively. Since the FC was optimised for collection of the 780 nm laser during alignment, it needed to be adjusted for the 810 nm output. This provides sufficient single count rates to then consider coincidence rates. The extra path length introduced on B and B' was accounted for by moving the delay onto A . The signal from detector A was then delayed by 12 ns to match those from B and B' . This resulted in coincidence counts being registered. After further tuning of the system, the typical count rates obtained were $N_B \sim 4000\text{ cps}$, $N_{B'} \sim 4000\text{ cps}$, and $N_{AB} + N_{AB'} \sim 140\text{ cps}$.

Polarisation dependence: A waveguide of length $7.47\text{ }\mu\text{m}$ was used. The polarisation angle was varied and the corresponding coincidence count rates were measured. Twelve measurements with integration time of 5 s were recorded for each angle. The angle was varied through $1\frac{1}{2}$ cycles. The resulting plot is shown in Fig. 5.8a.

Decay length: Ten measurements of output coincidence rates of eight waveguides of different lengths were recorded with an integration time of 24 s . The longer time was necessary to ensure noticeable reduction in coincidence rates at longer distances. Shorter waveguides ($L < 7\text{ }\mu\text{m}$) were not used as they had lower output counts rates. Figure 5.8b shows the decay plot for longer waveguides, while Fig. 5.8c shows that of shorter waveguides.

Spectral Response: Before beginning the characterisation measurements, a spectral response of the system was obtained. The spectra are shown in Fig. 5.6. The spectrum in Fig. 5.6a is slightly different from that shown Fig. 5.5a due to alignment variation of the fibre coupler which collects the output from the white laser.

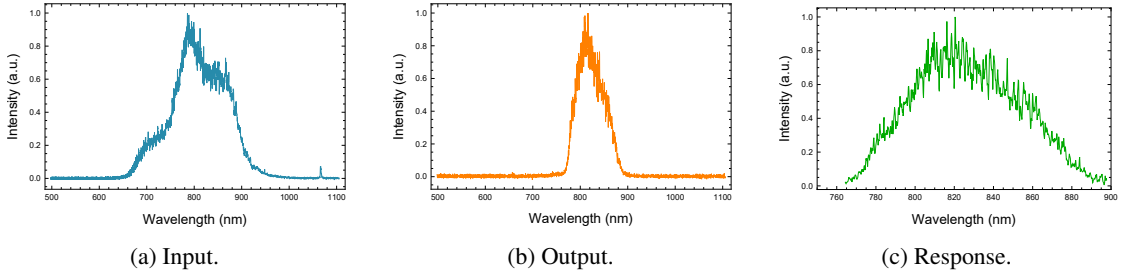


Figure 5.6: Spectral characterisation of a $p = 740\text{nm}$ grating. 5.6a Spectrum of input light from white laser. 5.6b Output spectrum from waveguide. 5.6c Spectral response of input-output grating combination.

The peak wavelength in the response is close to 810 nm , making the system suitable for the single-photon input.

Second-order coherence function $g^{(2)}(0)$: For this measurement, single-photons were coupled into a $7.47\mu\text{m}$ long waveguide with period $p = 740\text{ nm}$. Since the count rates were low, the triple coincidence rates $N_{ABB'}$ were most often zeros. Occasionally $N_{ABB'}$ would assume the value 1, and more rarely 2 or 3. This resulted in wild fluctuations of $g^{(2)}(0)$, but which can be mitigated with longer integration times. With this in mind, all count rates were recorded over a 2 hour period with an integration time of 1s . This allowed records to be grouped to form a measurement with longer integration time. The second-order coherence function was only determined for zero time delay, and is shown in Fig. 5.10. The long measurement time made recording several time delays impractical.

5.3 Results and Discussion

5.3.1 Classical

Polarisation dependence: The average and standard deviation of each set of ten measurements were calculated. The average count rates were plotted against the polarisation angle and is shown in Fig. 5.7a. The polarisation angle in this plot is relative to the waveguide orientation; a 90° polarisation is perpendicular to the SPP propagation direction. This was simply done by setting the angle of the first minimum to 90° . Then at 180° we expect a maximum and another minimum at 270° , as is seen in the plot. A function of the form $C(\theta) = a\cos^2(b\theta + c) + d$ was also fitted to the data to quantify how well it conforms to the \cos^2 form. The fit yielded a value of $r^2 = 0.99587$. The data demonstrates the expected behaviour well, indicating that only TM mode light is coupled into the SPP mode which is itself TM.

Decay length: The recorded powers for each waveguide length were averaged and then normalised. An exponential curve of the form $P(x) = e^{-b(x-x_0)}$ was fitted to the data. Here b is a parameter and x_0 is the length of the first waveguide. The decay length is then $\frac{1}{b} + x_0$. The fit yielded $r^2 = 0.99344$ and a decay length

$L = (16.83 \pm 0.04)\mu m$. The result (Fig. 5.8b) exhibits the expected exponential decay of SPP intensity, but the value of L is smaller than expected. This is most likely due to SPP leakage into the substrate. Furthermore, the surface of the waveguides have raised defects, as can be seen in Figs 5.1 and 5.4. These defects scatter light from the SPP mode as it propagate, thus resulting in a more rapid decay.

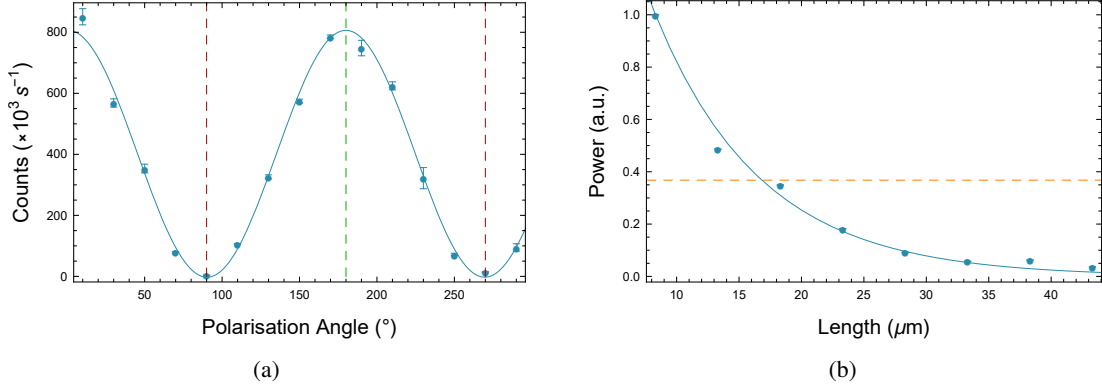


Figure 5.7: Classical SPP characterisation plots. (a) Polarisation dependence of in-coupling. (b) Exponential intensity decay.

5.3.2 Quantum

Polarisation dependence: The average and deviation of each data set was calculated and plotted. The result is shown in Fig. 5.8a. Similarly as in the classical case a \cos^2 curve is fitted to the data. With $r^2 = 0.9983$ and appropriate maxima and minima angles, the data clearly exhibits the typical behaviour.

Polarisation dependence and decay length: The data was processed in the same manner as the previous experiments. An exponential decay curve was fitted to the last seven data point. The plot of the data as well as fitted curves are shown in Fig. 5.8b. The fit yielded $r^2 = 0.9977$. The extracted decay length was ($L = 22.1 \pm 0.4$) μm . Once again, a smaller value than predicted was obtained. The same reasons apply here as in the classical case. It was decided that the first point be omitted from the fit as the curve appears to be non-exponential for lengths shorter than 12 μm . This was confirmed by probing shorter waveguides, the results of which can be seen in Fig. 5.8c. It is suspected that shorter waveguides become more cavity-like, distorting the SPP intensity profile. Additionally, simulations suggest that the SPP develops over a finite distance, after which the characteristic intensity decay becomes prevalent.

Second-order coherence function: The single count rates, have a tendency to drift as seen in Fig. 5.9. The fibre-couplers used for collection are sensitive around the optimal position. Temperature variations and vibrations can shift the fibre-core sufficiently to cause the observed drift. Being two orders of magnitude smaller than that of the count rates, the drift in N_A is negligible over the recorded period. A more noticeable drift is seen in N_B and $N_{B'}$ which is due to instability of the plasmonic chip mount. The efficiency of the

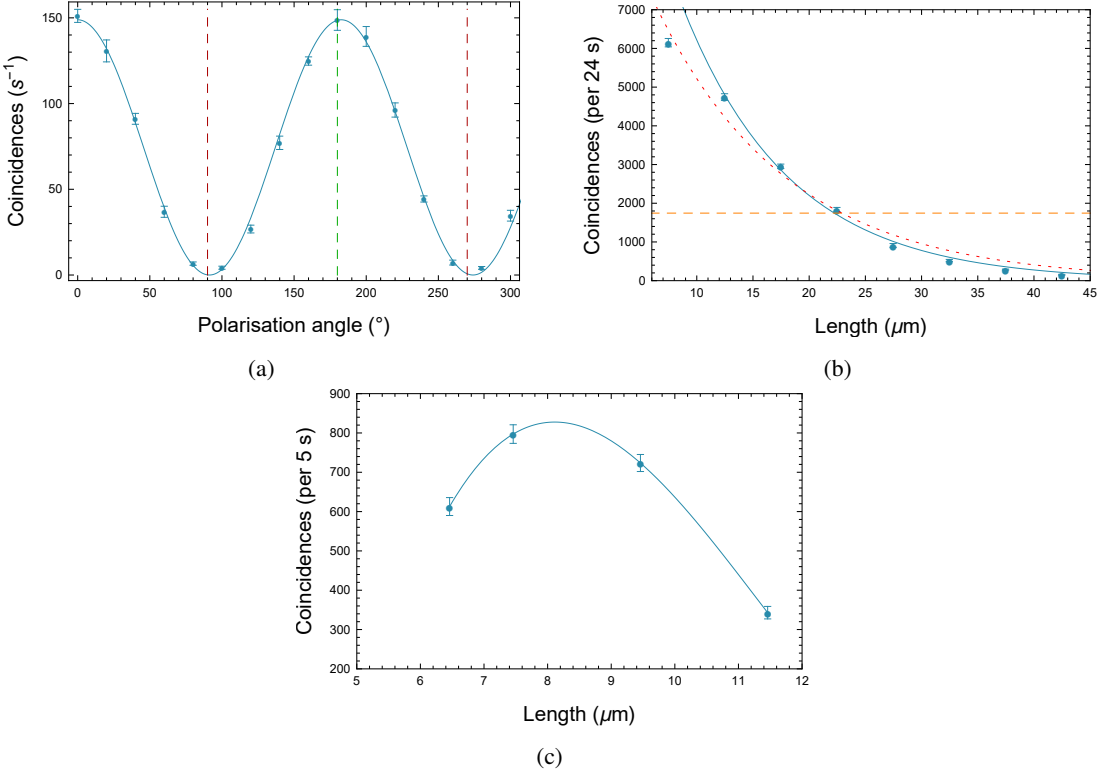


Figure 5.8: Single-SPP characterisation plots. (a) Polarisation dependence of in-coupling. (b) Exponential intensity decay. The dashed horizontal line indicates e^{-1} times the amplitude (count rate of th second point). The dashed exponential curve is the fit to all data point which has a lower $r^2 = 0.9887$. (c) Decay plot for shorter waveguides joined by an interpolating function. The second point has $L = 7.48\mu m$, this is only $0.01\mu m$ longer than than first point in (b).

photon-SPP coupling is sensitive to the position of the input on the grating. The input beam should be close to the edge of the grating next to the waveguide section. A few 100 nanometers off makes a significant difference. Ultimately, the drift in the single count rates appear to have little effect on the coincidence rates N_{AB} and $N_{AB'}$. The result of which is the stable average $g^{(2)}(0)$ seen in Fig. 5.10. The 7200 1 s records were grouped to form several sets. The records of each set were added to form a longer integration time. Using these summed records, $g^{(2)}(0)$ values were calculated and the average taken. This process was repeated for longer integration times (larger groups of 1s records). From Fig. 5.10 it can be seen that the error decreases rapidly. The grand mean of $g^{(2)}(0) = (0.160 \pm 0.002) < 0.5$ is in excellent agreement with the purely photonic value of (0.160 ± 0.008) . Thus the input photon number state is preserved. The error of the grand mean is a measure of the fluctuation in $g^{(2)}(0)$ across integration times, and is an order of magnitude smaller than the smallest error within an integration time.

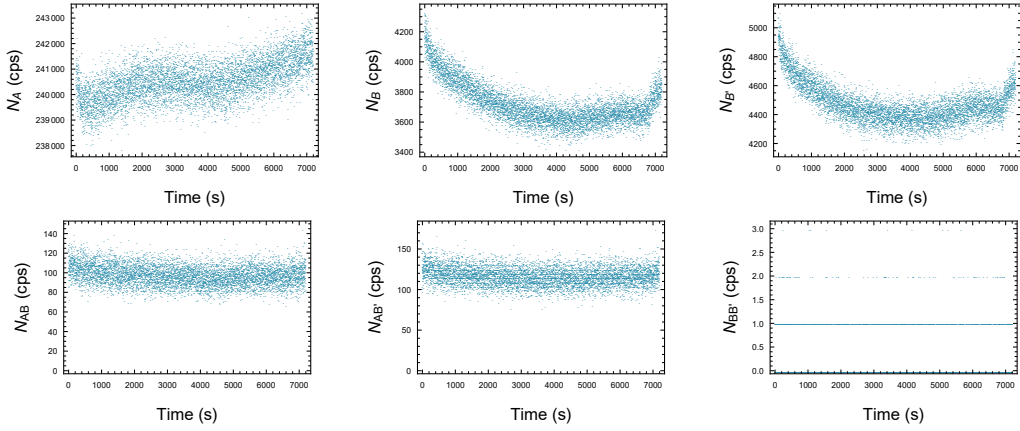


Figure 5.9: All count rates over the measurement period.

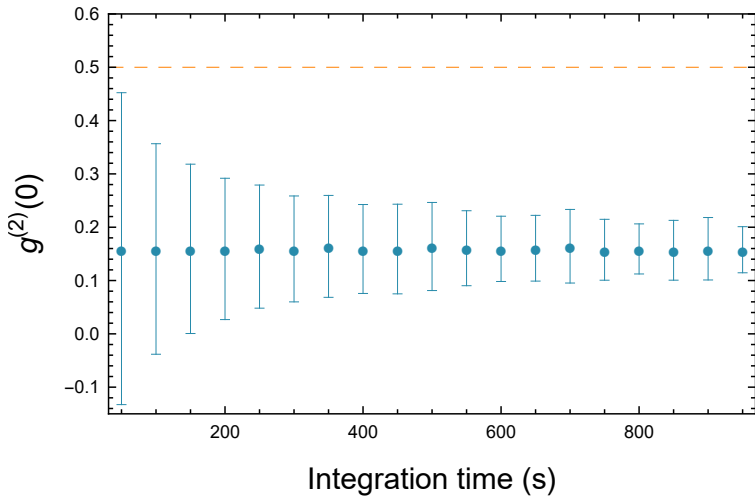


Figure 5.10: $g^{(2)}(0)$ as a function of integration time. The value of $g^{(2)}(0)$ is stable about a mean of 0.160 ± 0.008 . The standard deviation, however, rapidly decreases with increasing integration time.

5.4 Summary

In this chapter it was shown that SPPs were successfully excited of stripe waveguides in both the classical and quantum regimes. The main goal of demonstrating the photon-number preserving nature of SPPs was also achieved. An improvement that could be made in future would be the use of near-field scanning optical microscopy (SNOM) to map the SPP intensity profile. In this manner we can inspect the profile at short propagation distances while avoiding any cavity effects that arise from short waveguides. Additionally, a more direct measurement of the single-quanta nature of SPPs excited by single-photons could be made using a plasmonic beamsplitter in the HBT interferometer. This was not attempted in this work as the propagation distance in the beamsplitters were too long.

Chapter 6

Quantum Random Number Generation

6.1 Introduction

In this chapter we further strengthen the use of plasmonics for quantum information processing. We experimentally demonstrate a quantum random number generator using a plasmonic beamsplitter [47]. Quantum random number generators exploit the inherent randomness that is central to quantum mechanics, which makes them ideal sources of entropy. Using classical methods, true random number generation is hard to accomplish, as the unpredictability of the generation relies on an incomplete knowledge of a given system. On the other hand, in a quantum system true randomness is an essential part of the underlying quantum mechanics. True random numbers are important in many applications in science and technology, including in cryptography, simulation of economic, traffic and agricultural models, and for coordination in computer networks [50]. A device that generates true random numbers using quantum mechanics is therefore an important component.

Previously, single photons have been used as quantum generators of random numbers in bulk setups in various forms, including a branching path generator [51–53], time of arrival generator [54–56], photon counting generator [57–59] and many others [50]. Most recently on-chip quantum random number generators have been realised using one or more of the above methods [60–63]. In our experiment, we use the branching path method to generate random numbers quantum mechanically. We excite single SPPs on a gold stripe waveguide and scatter them into one of two possible outputs of a plasmonic beamsplitter. This enables a true random bit to be generated from the quantum scattering process. We then characterise the quality of the random number sequence generated, finding it to be comparable to other methods of photonic-based quantum

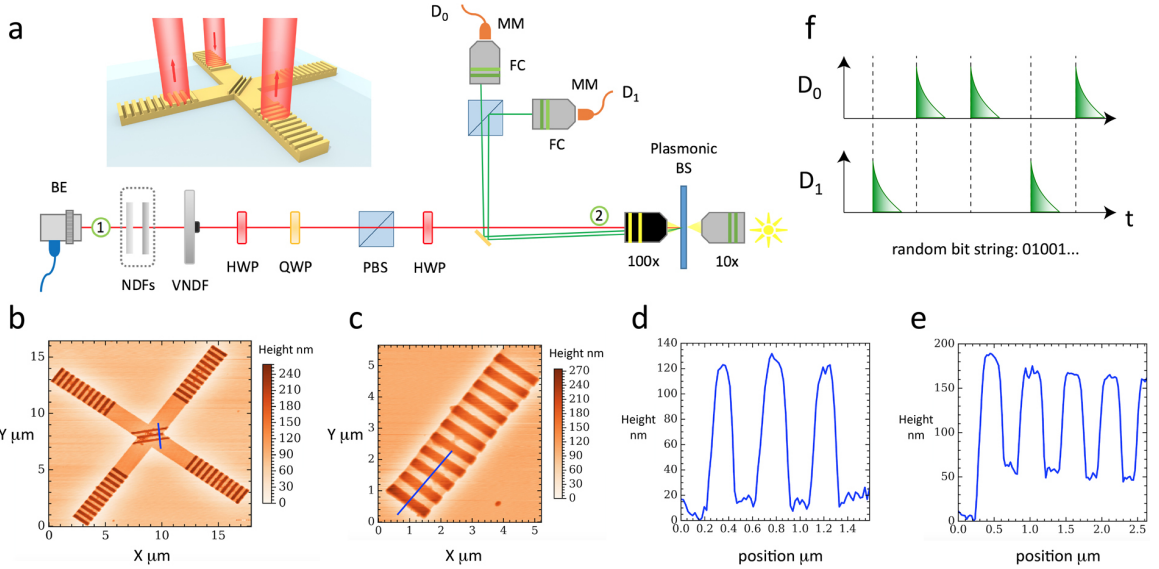


Figure 6.1: Quantum random number generation using a plasmonic beamsplitter. **a**, Microscope stage (inset illustration shows the input and output beam directions for the beamsplitter). The following labels are used: beam expander (BE), neutral density filters (NDFs), variable neutral density filter (VNDF), half-wave plate (HWP), quarter-wave plate (QWP), polarising beamsplitter (PBS), fibre coupler (FC), multimode fibre (MM), beamsplitter (BS) and detector (D). Coherent light is injected into the microscope stage via the BE and ND filters are used to attenuate it down to the single-photon level before being converted into single surface plasmon polaritons (SPPs). The presence of a single SPP input to the plasmonic beamsplitter is postselected by detection of a photon at either detector D_0 or D_1 , with a random bit being generated. The bit sequence generated from repeated runs originates from the quantum scattering process of single SPPs in the beamsplitter. **b**, Atomic force microscope (AFM) image of the beamsplitter. **c**, AFM image of the bottom left grating. **d**, AFM profile image of the splitting region (zero height set at waveguide level). **e**, AFM profile image of the grating region (zero height set at substrate level). **f**, An illustration of the detector pulses that signal the detection of a single photon at either beamsplitter output, leading to the generation of a random bit sequence (string).

random number generation [50]. The benefits of a plasmonic splitting device is that it is highly compact and therefore suitable for tight integration in an on-chip setting, where it could be used as a module in a quantum computing or quantum communication task.

6.2 Experimental Details

The setup used to investigate quantum random number generation using the plasmonic beamsplitter is shown in Fig. 6.1a, where a compound microscope is used to excite single SPPs on a plasmonic beamsplitter made from gold, illustrated in the inset of Fig. 6.1a. Each arm of the beamsplitter is $2\ \mu\text{m}$ in width and $70\ \text{nm}$ in height. At the ends of each arm and the intersection there is a surface-relief grating of height 90 nm . The end gratings serve as inputs and outputs for converting photons to SPPs and back again, with 11 steps of period $700\ \text{nm}$, while the centre grating with 3 steps of period of $500\ \text{nm}$ acts as a partial mirror, providing a splitting.

An SPP excited at one input grating propagates along the waveguide and upon reaching the central grating there is a probability that it is transmitted into the forward output and a probability that it is reflected into the perpendicular output. During propagation, the SPPs are highly confined to the surface of the waveguide, with a perpendicular characteristic length much less than the free-space wavelength [26, 35].

The beamsplitter is fabricated on a silica glass substrate of thickness 0.17 mm (refractive index $n = 1.5255$) by a combination of electron beam lithography (EBL) and electron beam evaporation (EBE). For the waveguide sections (layer 1, thickness 70 nm), a positive resist (electron-sensitive film) is spin coated on the substrate, with EBL used to define the waveguide regions. A lift-off technique is then used, with an adhesion layer of Ti (thickness 2-3 nm) deposited first and then the Au layer using EBE. The gratings (layer 2, thickness 90 nm) are formed similarly to the waveguides using alignment marks to match up layer 1 and 2. A three-dimensional image of the final beamsplitter structure is then obtained using an atomic force microscope (NT-MDT NTEGRA Prima), as shown in Figs. 6.1b-e.

To excite single SPPs in the beamsplitter a coherent light source in the form of a $\lambda = 780$ nm continuous-wave laser is used, operating above the lasing threshold at 35 mA. The light is injected into the microscope stage via a beam expander (BE). The collimated beam runs through a combination of two fixed and one variable neutral density (ND) filters, which are used to attenuate the coherent light down to the single-photon regime. The prepared source of light can be described by a weak coherent state $|\alpha\rangle = e^{-\frac{1}{2}|\alpha|^2} \sum_n \frac{\alpha^n}{\sqrt{n!}} |n\rangle$, with photon number distribution $P_n = e^{-|\alpha|^2} \frac{|\alpha|^{2n}}{n!}$ and $|\alpha|^2 = \langle \hat{n} \rangle \ll 1$ as the mean photon number. In this regime, the two dominant components are P_0 and P_1 . Using SPAD detectors for each output of the beamsplitter, the vacuum component P_0 is removed by postselection, *i.e.* when either detector clicks the quantum state injected into the input grating of the beamsplitter was a single-photon [53].

To clean up the polarisation of the input state, a polarising beam splitter (PBS) is used to select horizontally polarised photons, while a preceding quarter-wave plate (QWP) and half-wave plate (HWP) are used to control the incident polarisation. The beam is focused onto one input grating of the plasmonic beamsplitter (diffraction-limited spot) using a 100x microscope objective and its polarisation is adjusted using an additional HWP to maximise the in-coupling efficiency for conversion of photons to SPPs [26]. The two output modes of the beamsplitter are collected by the same objective, and are then picked-off by a knife-edge mirror and directed onto a PBS. This PBS separates the two orthogonally polarised outputs which are then coupled into multimode fibres that lead to separate SPAD detectors. The detectors are each connected to a channel of a Picoquant TimeHarp 260, which in turn is connected to a PC for data acquisition. In time-tagging mode the TimeHarp records the detector at which a photon arrives and its arrival time to a resolution of 25 ps.

In order to excite single SPPs we require that the average photon number n is much less than one per coherence time of the source [53]. The coherence time is given by $\tau = \sqrt{2\ln 2}/\pi\delta\nu$, where $\delta\nu$ is the frequency bandwidth of the laser [64]. Using $\delta\nu = 9.74$ THz we have $\tau = 3.85 \times 10^{-14}$ s. Thus the rate of photons injected into the plasmonic beamsplitter, R , must be much less than $1/\tau = 2.60 \times 10^{13}$ s⁻¹. The input rate in our setup was

calculated by measuring the power at position 1 in Fig. 6.1a and then measuring the transmission efficiency of all the optics between position 1 and 2. This yielded a transmission factor of $\eta = 2.78 \times 10^{-6}$. With the power at position 1 as $P_1 = 1.23$ mW and multiplying it by η we obtain an input power of $P_{in} = 3.77 \times 10^{-9}$ W into the microscope objective. Dividing this by the average photon energy gives $R \simeq \frac{4P_{in}}{hc} = 1.47 \times 10^{10}$ s $^{-1}$. While this is clearly much less than $1/\tau$, an additional constraint comes from the SPAD detector dead time $\tau_d = 24$ ns [50, 65]. If a detector detects a photon it will not detect another within this time. Thus for 2 photons arriving within τ_d only one will be detected. This leads to an excess of substrings 01 and 10, as the detectors miss the substrings 00 and 11 at random places [65]. The input power is therefore set using a variable ND filter so that the detected rate in each detector is 1.2×10^6 s $^{-1} \ll 1/\tau_d = 4.2 \times 10^7$ s $^{-1}$.

The detection of photons from the plasmonic beamsplitter outputs produce signals in the form of pulses from the SPADs, as illustrated in Fig. 6.1f. These signals are sent to the TimeHarp which records the arrival times of the pulses from both channels and from this we extract a random binary sequence. The sequence is constructed by denoting a pulse from detector 0 as the binary digit 0 and a pulse from detector 1 as the digit 1. A total of 82,604,923 binary digits (bits) were acquired over a 34 s period, corresponding to a rate of 2.43 Mbits/s.

6.3 Initial Characterisation

We characterise our random bit sequence by applying a number of standardised tests [50, 53]. These tests are employed to determine if the generated sequence exhibits characteristics typical of a true random bit sequence. In what follows we describe the tests performed on a sample of 80 Mbits and present the results:

(i) Autocorrelation: We first calculate the correlation coefficients [66] of the bit sequence with itself up to a 31-bit delay in order to examine any short-ranged correlations and periodicity. The coefficients lie in the interval [-1, 1]. A value of 1 and -1 indicate correlation and anti-correlation respectively, while a value of 0 suggests uncorrelated bits. Fig. 6.2a is a plot of the obtained coefficients, and shows only a small negative correlation between adjacent bits, after which the correlation remains consistently close to zero. The inset shows a zoomed in region that omits the first data point in order to emphasise the lower lying points. The negative correlation can be seen, as well as a small positive correlation for delays greater than one bit. The main sources of these residual correlations in a beamsplitter scenario can be attributed to a combination of detector dark counts, deadtime and afterpulsing in the SPADs [65, 67].

(ii) Uniform distribution of n -bit blocks: For a true random bit sequence, all possible n -bit combinations should be equally probable. We consider single bits and 8-bit blocks. In the case of single bits we should have an equal number of zeros and ones for a large enough sample. For 8-bit blocks that are converted to unsigned integers, we expect a uniform distribution of occurrences over the domain [0, 255]. Furthermore,

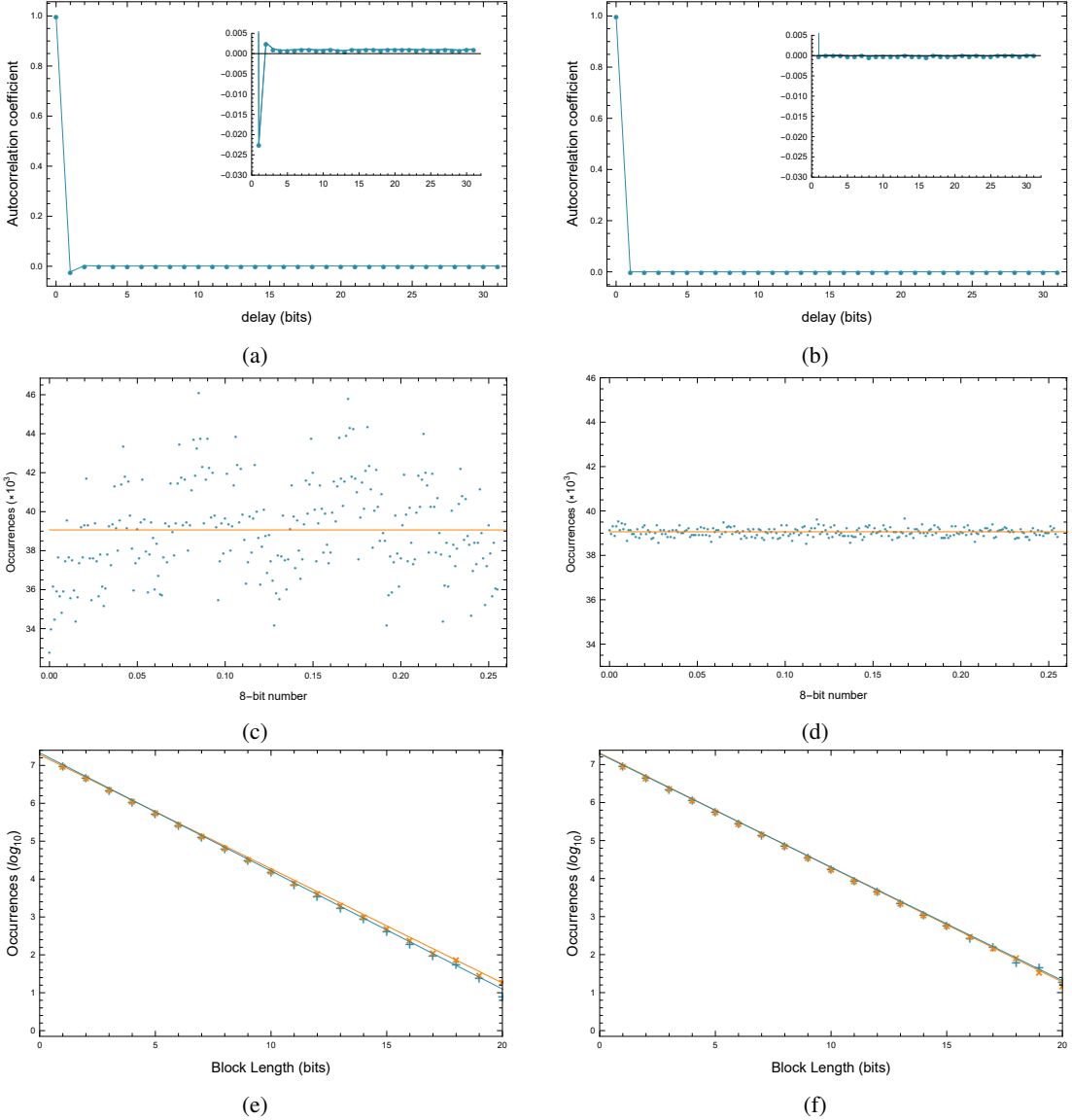


Figure 6.2: Characterisation of generated random bit sequence. (a), (b) Autocorrelation coefficient. Inset shows zoomed region to highlight residual correlation. (c), (d) Distribution of 8-bit blocks (bytes). (e), (f) Distribution of run lengths of ones (x) and zeros (+). (a), (c), and (e) are the characterisation results of the unprocessed bit sequence. (b), (d), and (f) are the results for the post-processed bit sequence.

the average must approach the value of 127.5. Using our 80 Mbit sample we find the proportion of ones as 0.5023 and zeros as 0.4977, showing a small bias towards one. The distribution of 8-bit integers is shown in Fig. 6.2c. The average of the 10×10^6 integers is 128.13, which is slightly larger than expected due to the small bias and residual correlations in the sequence.

(iii) Distribution of run lengths: A run is a continuous string of zeros or ones. If finding a zero or a one are equally likely then the probability of finding a run of n -bits is proportional to 2^{-n} . Fig. 6.2e shows the run length distributions for both zeros and ones. Fitting a straight line to the first twenty points gives a gradient

of (-0.312 ± 0.001) for runs of zeros, and (-0.301 ± 0.002) for runs of ones. The ideal values should be $-\log_{10} 2 \simeq -0.301$. The discrepancy in the case of runs of zeros is due to the smaller probability of obtaining a zero as a result of bias. The smaller probability results in a higher likelihood of obtaining a run of ones than a run of zeros of the same length. This in turn contributes to the small periodic character of the 8-bit integer distribution shown in Fig. 6.2c.

(iv) The entropy of an n -bit string: This is defined as $-\sum_i p_i \log_2 p_i$, where $i \in \{0, 1\}^n$ and p_i is the probability of obtaining i . The entropy can be used as a measure of irregularity. A perfectly random source of n -bit strings should have n bits of entropy. A value of 7.99726 bits was calculated for 8-bit strings using the probabilities obtained from the distribution in Fig. 6.2c.

(v) Estimation of π : As a more functional check we estimated the value of π using a Monte Carlo method. Here the area of a circle of radius r divided by the area of a square with sides of length $2r$ is equal to $\pi/4$. Thus, by populating a quadrant of the square with enough randomly placed points and finding the ratio of points within the quarter-circle to the total, we arrive at an estimate of 3.13366 for π .

6.4 Post-processing

Due to a slight asymmetry of the beamsplitter and functionality of the SPADs, the bit strings produced exhibit small short-ranged correlations amongst bits, as shown in Fig. 6.2a, and a bias in the form of non-uniform single-bit and 8-bit distributions, as shown in Figs. 6.2c. To mitigate these effects we employ a randomness extractor to the bit sequence [50]. The extractor applied here is an extension of the von Neumann scheme [68, 69] and was chosen for its simplicity and non-use of a random seed. The algorithm proposed by von Neumann can be applied to a biased generator of independent bits. Such a generator would produce a 0 and a 1 with respective probabilities of p and q with $p \neq q$. Since the bits are independent, the bit-pairs 01 and 10 occur with an equal probability of pq . Thus, occurrences of these pairs can serve as an unbiased source of random bits. This is done by assigning a 0 bit when a 01 pair is produced, and a 1 for 10 pairs. A biased input will therefore be reduced to a fraction pq of its original length. An extension of this scheme described in Ref. [69] overcomes the reduction by producing further biased sequences from the original sequence, to which the von Neumann algorithm is then applied. This procedure is repeated recursively with each output being concatenated to the previous. Before applying the recursive algorithm we require that adjacent pairs of bits be uncorrelated. From the autocorrelation plot in Fig. 6.2a it is clear that a fraction of adjacent bits are anti-correlated. To minimise this correlation we first shuffle the sequence and then apply the recursive von Neumann algorithm. Applying the algorithm to 32 sequences of 2.4 Mbits yielded an average output of 2.3682 ± 0.0003 Mbits, leading to a marginally reduced generation rate of 2.37 Mbits/s.

6.5 Results

The tests described above are then applied to the post-processed sequence, which we denote as QRNG. For comparison, a sequence of equal length obtained from the Marsaglia CD-ROM [70] was also tested. The sequence was generated using a combination of pseudorandom number generators. We denote this sequence as PRNG. A summary of the results are given in Tab. 6.1, where we have also included the results from the quantum photonic implementation of Ref. [53]. The detailed results for the QRNG sequence are shown in Figs. 6.2b, d, and f. There is clearly an improvement that can be seen in the results of the tests. The autocorrelation varies by a maximum of ~ 0.0002 over the bit delay range, the distribution of bytes is markedly improved and the distribution of block lengths of zeros and ones match up for larger block sizes. As a further and more rigorous test we apply the NIST Statistical Test Suite (STS) to the QRNG and PRNG sequences. The NIST test suite is aimed at becoming the first industry standard for testing random numbers and a detailed description of the tests can be found in Ref. [71]. The PRNG sequence fails the NIST test suite (Longest run of ones and Overlapping template matching tests are not passed), while the QRNG sequence passes all tests at the 1% significance level, performing well compared to other quantum photonic-based implementations [50, 55, 57, 60, 65, 72, 73]. A summary of the results of the NIST tests is given in Tab. 6.2. The Overlapping Template Matching, Linear Complexity, Random Excursion, and Random Excursion Variant tests were run on a set of 80 sequences of 1 Mbits in length. The remaining tests ran on 160 sequences of length 500 Kbits.

6.6 Discussion

In this work we demonstrated the generation of random numbers using a plasmonic beamsplitter operating in the quantum regime. The presence of a plasmonic excitation in a given output from the beamsplitter determined the value of a random bit generated from a quantum scattering process. Using a stream of single plasmons we achieved a quantum random number generation rate of 2.42 Mbits/s, despite the presence of loss in the waveguides. We characterised the quality of the random number sequence generated and with post-processing found it to be comparable in quality to sequences from other photonic-based devices. Higher generation rates in our setup may be achieved in a number of ways: the use of detectors with reduced dead-times [57], operating several beamsplitters in parallel and including additional degrees of freedom such as

	Mean	Entropy	π
QRNG	127.49	7.999981	3.13227
QRNG [53]	127.50	7.999965	3.14017
PRNG	127.50	7.999982	3.13252

Table 6.1: Summary of results from tests applied to the post-processed and PRNG sequences.

the excitation arrival time [50, 65]. Improvements in the fabrication of the beamsplitter would also reduce the bias between ones and zeros, and together with detector improvements would remove the need for post-processing which adds an additional resource overhead. The compact nature of the beamsplitter makes it suitable for integration in a variety of on-chip applications, such as in quantum computing and communication schemes. Future work into the integration of high quality sources and detectors on-chip would enable a fully self-contained device for use in a range of applications where true random number generation is required.

Statistical Test	p-value	Proportion/Threshold	Pass
Frequency	0.546791	156/154	Yes
Block Frequency	0.624107	159/154	Yes
Cumulative sums	0.606531	158/154	Yes
Runs	0.371101	159/154	Yes
Longest run	0.284375	159/154	Yes
Rank	0.162606	158/154	Yes
FFT	0.947557	157/154	Yes
NonOverlappingTemplate	0.723759	158/154	Yes
OverlappingTemplate	0.559523	79/76	Yes
Universal	0.330628	159/154	Yes
Approximate Entropy	0.350485	157/154	Yes
Random Excursions	0.516893	44/42	Yes
Random Excursions Variant	0.054933	45/42	Yes
Serial	0.606531	160/154	Yes
Linear Complexity	0.392456	79/76	Yes

Table 6.2: Summary of results from the NIST tests applied to the post-processed sequence QRNG. The p-value is the probability a perfect random number generator would generate the particular experimental result or a result indicating a less random bit sequence. If $p > 0.01$, the significance level, the bit sequence passes the test. Proportion is the proportion of the tested sequences that succeed in passing a test.

Chapter 7

Summary

We have described SPPs in the classical regime. From this description we identified three SPP characteristics: the evanescent confinement to the interface, exponential decay with propagation distance, and that they are transverse-magnetic. We also arrived at the SPP dispersion relation which reveals the momentum mismatch between photons and SPPs of the same frequency. This necessitated a look at photon-to-SPP coupling schemes. A more detailed study of grating couplers was carried out with the aid of simulations. This entailed an optimisation of the input grating, which yielded an optimal period of 740 nm and 710 nm for input wavelengths of 810 nm and 780 nm respectively. The optimal height was 60 nm , and duty-cycle was between 0.4 and 0.5 for both wavelengths. Output grating simulations showed that a duty-cycle of 0.5 and a slightly smaller height of 55 nm makes for a more efficient output grating. It was also seen that any period at least 10 nm smaller than the optimal input period serves well. However, it should be noted that the output beam becomes increasingly angled towards the input grating with smaller periods ($< 600\text{ nm}$). These results were important as they allowed us to choose the best input grating period for each wavelength of interest. The only available height and duty-cycle were 90 nm and 0.5 respectively, and the output gratings were identical to their corresponding input gratings. These proved sufficient to experimentally demonstrate the TM mode restriction of SPPs and their exponential decay in both the classical and quantum regime. These measurements were achieved using a compound microscope stage.

Following the classical description of SPPs was a brief prescription for quantising SPPs, in which their bosonic nature comes to light. The question then arises, do single photons excite single SPPs and remain as single excitations upon decoupling? To show this, we first built a single-photon source and characterised the photonic state it generated by measuring $g^{(2)}(0)$. The result was $g^{(2)}(0) = 0.0160 \pm 0.008$ indicating single photon states. Then, the same measurement was performed on the output of a plasmonic stripe waveguide on which single SPPs were excited by single photons. The value obtained was $g^{(2)}(0) = 0.0160 \pm 0.002$, which agrees well with the photonic value. Hence, we can conclude that SPPs preserve the photon-number statistics

of their exciting photons.

We have discussed the advantages of quantum plasmonics for QIPC applications, and methods of dealing with its major drawback - loss. Much work is still needed in this area, but we demonstrated a simple protocol where loss does not need to be circumvented. We showed that random bit sequences can be generated using the branching-path method with single SPPs. The advantage of this is that plasmonic devices (in this case a beam splitter) can be miniaturised much further than dielectric devices.

The aim of the project was to acquire the experimental capacity and skills needed to undertake further classical and quantum plasmonics research. This goal has been achieved as shown by the demonstrations summarised above. In performing this study, experimental setups, and electronic, optical and mechanical components have been acquired. These resources will be crucial in future studies. The next step is the investigation of nitrogen-vacancy centres (NV-centres) in diamond nanoparticles for QIPC applications. A natural starting point would be the study of NV-centres coupled to plasmonic waveguides and antennas. The first such experiment would involve the characterisation of NV-centres directly excited by free-propagating light. Two of characteristics to be verified would be:

1. The single-photon nature of the emitted light via a measurement of the second-order coherence function $g^{(2)}(\tau)$,
2. and the emission-time distribution, from which we may obtain the NV-centre decay rate which characterises the coupling efficiency.

These measurements will make use of the microscope stage, single-photon counting electronics, and the skills that have now been established. The same measurements can then be done for classical SPPs coupled to NV-centres which in turn decouple into single-SPP modes. With suitable NV-centres identified and characterised, our attention will turn to designing waveguides and antennas that provide useful effects for QIPC, such as plasmonic transistors [74]. The design process will make good use of the simulation skills thus far acquired. Once a promising design arises, it will be fabricated using the lithography capability of the available AFM. These experiments will enable further study of the quantum dynamics of dissipative emitter-cavity systems in a plasmonic setting. This is the ultimate goal.

Bibliography

- [1] S. A. Maier, Plasmonics: Fundamentals and Applications, (Springer, New York, 2007).
- [2] J. Takahara, S. Yamagishi, H. Taki, A. Morimoto and T. Kobayashi, Guiding of a one-dimensional optical beam with nanometer diameter, *Opt. Lett.* **22**, 475 (1997).
- [3] J. Takahara, in Plasmonic Nanoguides and Circuits (ed. Bozhevolnyi, S. I.) Ch. 2 (Pan Stanford Publishing, 2009).
- [4] S. Kawata, Y. Inouye and P. Verma, Plasmonics for near-field nano-imaging and superlensing, *Nature Photonics* **3**, 388 (2009).
- [5] E. Abbe, Beiträge zur Theorie des Mikroskops und der mikroskopischen Wahrnehmung. *Arch. mikrosk. Anat. Entwicklungsmech* **9**, 413-648 (1873).
- [6] I. I. Smolyaninov, C. C. Davis, J. Elliott and A. V. Zayats, Resolution enhancement of a surface immersion microscope near the plasmon resonance. *Opt. Lett.* **30**, 382-384 (2005).
- [7] J. Homola, S. S. Yee and G. Gauglitz, Surface plasmon resonance sensors: review, *Sensors and Actuators B* **54**, 3 (1999).
- [8] J. N. Anker, W. Paige Hall, O. Lyandres, N. C. Shah, J. Zhao and R. P. Van Duyne, Biosensing with plasmonic nanosensors, *Nature Materials* **7**, 442 (2008).
- [9] E. Ozbay, Plasmonics: Merging photonics and electronics at nanoscale dimensions, *Science*, **311**, 189 (2006).
- [10] C. M. Soukoulis and M. Wegener, Past achievements and future challenges in the development of three-dimensional photonic metamaterials, *Nature Photonics* **5**, 523 (2011).
- [11] N. Meinzer, W. L. Barnes, and I. R. Hooper, Plasmonic meta-atoms and metasurfaces, *Nature Photon.* **8**, 889 (2014).
- [12] M. S. Tame, K. R. McEnergy, Ş. K. Özdemir, S. A. Maier and M. S. Kim, Quantum Plasmonics, *Nature Physics* **9**, 329 (2013).

- [13] I. Aharonovich, S. Castelletto, D. A. Simpson, C.-H. Su, A. D. Greentree and S. Prawer, Diamond-based single-photon emitters. *Rep. Prog. Phys.* **74**, 076501 (2011).
- [14] S. Buckley, K. Rivoire and J. Vuckovic, Engineered quantum dot single-photon sources, *Rep. Prog. Phys.* **75**, 126503 (2012).
- [15] A. V. Akimov, A. Mukherjee, C. L. Yu, D. E. Chang, A. S. Zibrov, P. R. Hemmer, H. Park, M. D. Lukin, Generation of single optical plasmons in metallic nanowires coupled to quantum dots. *Nature* **450**, 402-406 (2007).
- [16] R. Kolesov, B. Grotz, G. Balasubramanian, R. J. Sthr, A. A. L. Nicolet, P. R. Hemmer, F. Jelezko and J. Wrachtrup, Wave-particle duality of single surface plasmon polaritons. *Nature Phys.* **5**, 470-474 (2009).
- [17] A. Huck, S. Kumar, A. Shakoor and U. L. Andersen, Controlled coupling of single nitrogen-vacancy center to a silver nanowire. *Phys. Rev. Lett.* **106**, 096801 (2011).
- [18] A. Cuche, O. Mollet, A. Drezet and S. Huant, ‘Deterministic’ quantum plasmonics, *Nano Letters* **10** , 4566-4570 (2011).
- [19] Birnbaum, K. M. et al. Photon blockade in an optical cavity with one trapped atom. *Nature* **436**, 87-90 (2005).
- [20] D. E. Chang, A. S. Srensen, E. A. Demler, M. D. Lukin, A single-photon transistor using nanoscale surface plasmons. *Nature Phys.* **3**, 807-812 (2007).
- [21] P. Kolchin, R. F. Oulton and X. Zhang, Nonlinear quantum optics in a waveguide: Distinct single photons strongly interacting at the single atom level. *Phys. Rev. Lett.* **106**, 113601 (2011).
- [22] D. E. Chang, V. Vuletic and M. D. Lukin, Quantum nonlinear optics - photon by photon. *Nature Photon.* **8**, 685-694 (2014).
- [23] E. Altewischer, M. P. van Exter and J. P. Woerdman, Plasmon-assisted transmission of entangled photons. *Nature* **418**, 304-306 (2002).
- [24] S. Fasel, F. Robin, E. Moreno, D. Erni, N. Gisin and H. Zbinden, Energy-time entanglement preservation in plasmon-assisted light transmission. *Phys. Rev. Lett.* **94**, 110501 (2005).
- [25] X. F. Ren, G. P. Guo, Y. F. Huang, C. F. Li and G. C. Guo, Plasmon-assisted transmission of high-dimensional orbital angular-momentum entangled state. *Europhys. Lett.* **76**, 753-759 (2006).
- [26] G. Di Martino, Y. Sonnefraud, S. Kéna-Cohen, M. S. Tame, Ş. K. Özdemir, M. S. Kim and S. A. Maier, Quantum statistics of surface plasmon polaritons in metallic stripe waveguides, *Nano Letters* **12**, 2504-2508 (2012).

- [27] C. C. Gerry and P. L. Knight, *Introductory Quantum Optics*, (Cambridge University Press, Cambridge, 2005).
- [28] J. J. Thorn, M. S. Neal, V. W. Donato, G. S. Bergreen, R. E. Davies, and M. Beck, Observing the quantum behaviour of light in an undergraduate laboratory, *Am. J. Phys.* **72**, 1210-1219 (2004).
- [29] R. Loudon, *The Quantum Theory of Light*, 3rd edition, (Oxford University Press, Oxford, 2000).
- [30] S. Bettelli, Comment on "Coherence measures for heralded single-photon sources", *Phys. Rev. A* **81**, (2010).
- [31] C. K. Hong, Z. Y. Ou, and L. Mandel, Measurement of Subpicosecond Time Intervals between Two Photons by Interference, *Phys. Rev. Lett.* **59**, 2044 (1987).
- [32] J. S. Fakonas, H. Lee, Y. A. Kelaita and H. A. Atwater, Two-plasmon quantum interference. *Nature Phot.* **8**, 317-320 (2014).
- [33] G. Fujii, D. Fukuda and S. Inoue, Direct observation of bosonic quantum interference of surface plasmon polaritons using photon-number-resolving detectors. *Phys. Rev. B* **90**, 085430 (2014).
- [34] Y.-J. Cai, M. Li, X.-F. Ren, C.-L. Zou, X. Xiong, H.-L. Lei, B.-H. Liu, G.-P. Guo and G.-C. Guo, High visibility on-chip quantum interference of single surface plasmons. *Phys. Rev. App.* **2**, 014004 (2014).
- [35] G. Di Martino, Y. Sonnefraud, M. S. Tame, S. Kéna-Cohen, F. Dieleman, Ş. K. Özdemir, M. S. Kim, S. A. Maier, Observation of quantum interference in the plasmonic Hong-Ou-Mandel effect. *Phys. Rev. Applied* **1**, 034004 (2014).
- [36] A. González-Tudela, D. Martín-Cano, E. Moreno, L. Martin-Moreno, C. Tejedor and F. J. Garca-Vidal, Entanglement of Two Qubits Mediated by One-Dimensional Plasmonic Waveguides. *Phys. Rev. Lett.* **106**, 020501 (2011).
- [37] J. Hou, K. Słowiak, F. Lederer and C. Rockstuhl, Dissipation-driven entanglement between qubits mediated by plasmonic nanoantennas. *Phys. Rev. B* **89**, 235413 (2014).
- [38] C. Lee, M. Tame, C. Noh, J. Lim, S. A. Maier, J. Lee, D. G. Angelakis, Robust-to-loss entanglement generation using a quantum plasmonic nanoparticle array. *New J. Phys.* **15**, 083017 (2013).
- [39] G. W. Hanson, S. A. H. Gangaraj, C. Lee, D. G. Angelakis, M. Tame, Quantum plasmonic excitation in graphene and robust-to-loss propagation. *Phys. Rev. A* **92**, 013828 (2015).
- [40] C. Lee, F. Dieleman, J. Lee, C. Rockstuhl, S. A. Maier, M. S. Tame, Quantum plasmonic sensing: beyond the shot-noise and diffraction limit. *ACS Photonics* **3**, 992 (2016).
- [41] P. B. Johnson and R. W. Christy, Optical constants of the noble metals, *Phys. Rev. B*, 43704379 (1972).

- [42] A. D. Rakić, A. B. Djurišić, J. M. Elazar, and M. L. Majewski, Optical properties of metallic films for vertical-cavity optoelectronic devices, *App. Opt.* **37**, 5271-5283 (1998).
- [43] I. R. Hooper and J. R. Sambles ,Dispersion of surface plasmon polaritons on short-pitch metal gratings, *Phys. Rev. B* **65**, 165432 (2002).
- [44] I. R. Hooper and J. R. Sambles ,Dispersion of surface plasmon polaritons on short-pitch metal gratings, *Phys. Rev. B* **65**, 165432 (2002).
- [45] E. Kretschmann and H. Raether, Radiative Decay of Non Radiative Surface Plasmons Excited by Light, *Z. Naturforsch.* **23A**, 2135 (1968).
- [46] A. Archambault, F. Marquier, and J. Greffet, Quantum theory of spontaneous and stimulated emission of surface plasmons, *Phys. Rev. B* **82**, 035411 (2010).
- [47] J. T. Francis, X. Zhang, S. K. Özdemir, and M. S. Tame, Quantum random number generation using an on-chip plasmonic beamsplitter, *arXiv:1610.06300* (2016).
- [48] M. S. Tame, C. Lee, D. Ballester, M. Paternostro, A. V. Zayats, and M. S. Kim, Single-Photon Excitation of Surface Plasmon Polaritons, *Phys. Rev. Lett.* **101**, 190504 (2008).
- [49] J. Jin, *The finite element method in electromagnetics*, (John Wiley & Sons, 2014).
- [50] M. Herrero-Collantes and J. C. Garcia-Escartin, Quantum random number generators, *arXiv:1604.03304* (2016).
- [51] J. G. Rarity, P. C. M. Owens and P. R. Tapster, Quantum random number generation and key sharing, *J. Mod. Opt.* **41**, 2435-2444 (1994).
- [52] A. Stefanov, N. Gisin, O. Guinnard, L. Guinnard and H. Zbinden, Optical quantum random number generator, *J. Mod. Opt.* **47**, 595-598 (2000).
- [53] T. Jennewein, U. Achleitner, G. Weihs, H. Weinfurter and A. Zeilinger, A Fast and Compact Quantum Random Number Generator, *Rev. Sci. Instrum.* **71**, 1675 (2000).
- [54] H.-Q. Ma, Y. Xie and L.-A. Wu, Random number generation based on the time of arrival of single photons, *App. Opt.* **44**, 7760 (2005).
- [55] M. Stipčević and B. M. Rogina, Quantum random number generator based on photonic emission in semiconductors, *Rev. Sci. Instrum.* **78**, 045104 (2007).
- [56] L. M. Yu, M. J. Yang, P. X. Wang and S. Kawata, Note: A sampling method for quantum random bit generation, *Rev. Sci. Instrum.* **81**, 046107 (2010).
- [57] M. Furst, H. Weier, S. Nauerth, D.G. Marangon, C. Kurtsiefer and H. Weinfurter, High speed optical quantum random number generation, *Opt. Exp.* **18**, 13029-13037 (2010).

- [58] M. Ren, E. Wu, Y. Liang, Y. Jian, G. Wu and H. Zeng, Quantum random-number generator based on a photon-number-resolving detector, Phys. Rev. A **83**, 023820 (2011).
- [59] E. de J. Lopes Soares, F. A. Mendonca and R. V. Ramos, Quantum Random Number Generator Using Only One Single-Photon Detector, IEEE Phot. Tech. Lett. **26**, 851-853 (2014).
- [60] B. Sanguinetti, A. Martin, H. Zbinden and N. Gisin, Quantum Random Number Generation on a Mobile Phone, Phys. Rev. X **4**, 031056 (2014).
- [61] A. Khanmohammadi, R. Enne, M. Hofbauer and H. Zimmermann, A Monolithic Silicon Quantum Random Number Generator Based on Measurement of Photon Detection Time, IEEE Phot. J. **7**, 1-13 (2015).
- [62] S. Tisa, F. Villa, A. Giudice, G. Simmerle and F. Zappa, High-Speed Quantum Random Number Generation Using CMOS Photon Counting Detectors, IEEE J. Sel. Top. Quant. Electron. **21**, 23-29 (2015).
- [63] C. Abellan *et al.*, Quantum entropy source on an InP photonic integrated circuit for random number generation, Optica **3**, 989 (2016).
- [64] B. E. A. Saleh and M. C. Teich, Fundamentals of Photonics, 2nd edition, Wiley.
- [65] M. Stipčević and J. E. Bowers, Spatio-temporal optical random number generator, Opt. Exp. **23**, 11619 (2015).
- [66] A. L. Edwards, The Correlation Coefficient, Ch. 4 in An Introduction to Linear Regression and Correlation. San Francisco, CA: W. H. Freeman, pp. 33-46 (1976).
- [67] M. Stipčević and R. Ursin, An On-Demand Optical Quantum Random Number Generator with In-Future Action and Ultra-Fast Response, Sci. Rep. **5** 10214 (2015).
- [68] J. von Neumann, Various techniques used in connection with random digits, National Bureau of Standards Applied Mathematics Series **12**, 36-38 (1951).
- [69] Y. Peres, Iterating Von Neumann's Procedure for Extracting Random Bits, Annals of Statistics **20**, 590-579 (1992).
- [70] G. Marsaglia, The Marsaglia Random Number CDROM, Department of Statistics and Supercomputer Computations Research Institute, Florida State University (1995). Available at <http://stat.fsu.edu/pub/diehard>.
- [71] NIST STS test available at <https://code.google.com/archive/p/randomnumbertestsuite-nist>.
- [72] W. Wei and H. Guo, Bias-free true random-number generator, Opt. Lett. **34**, 1876 (2009).

- [73] Y.-Q. Nie, H.-F. Zhang, Z. Zhang, J. Wang, X. Ma, J. Zhang and J.-W. Pan, Practical and fast quantum random number generation based on photon arrival time relative to external reference, *Appl. Phys. Lett.* **104**, 051110 (2014).
- [74] D. E. Chang, A. S. Sørensen, E. A. Demler, and M. D. Lukin, A single-photon transistor using nanoscale surface plasmons, *Nat. Phys.* **3**, 807-812 (2007).